Modeling and Stability Analysis of Fuel Cell-Based Marine Hybrid Power Systems

Nastaran Shakeri, *Student member, IEEE*, Wenjie Chen, *Student member, IEEE*, Mehdi Zadeh, *Senior Member, IEEE*, Ahmed Abdelhakim, *Senior Member, IEEE*, Asgeir J. Sørensen, *Senior Member, IEEE*, and Kang Tai

***Abstract*—This article proposes a framework for stability analysis of hydrogen fuel cell-based hybrid power systems (HPS) for zero-emission propulsion. An analytical model is developed and a comprehensive modal analysis is performed to address the HPS dynamic interactions. Sensitivity analysis assesses the impact of operating conditions, control parameters of the governor and converter controllers, and different control strategies. The case studies focus on how the parameters of the HPS state variables are coupled with the HPS modes through participation factors (PFs), thereby emphasizing which system state participates in determining the system's dynamics. The modal analysis characterizes the influence of control parameters on poorly damped modes, and enables expanding the stable operating region of the HPS by appropriate control parameter selection. The results indicate a notable impact of the voltage control loop parameters on the system stability, a strong coupling between the subsystems' current state variables and dc bus voltage dynamics, and a strong coupling between the governor dynamics and the FC current state. Additionally, the study demonstrates a PF of 0.9 between the dc bus voltage and the HPS's critical modes within 15% deviation by changes in the voltage controller's proportional gain. Finally, analytical analysis and time-domain simulations are validated with a real-time hardware-in-the-loop (HIL) test setup.**

***Index Terms*—Batteries, fuel cells, hydrogen, marine power systems, modeling, onboard power systems, propulsion, stability.**

I. Introduction

ELECTRIFICATION is a key enabler for the realization of a sustainable transformation in the maritime sector and the integration of autonomous systems. Maritime transportation contributes nearly 3% of annual global greenhouse gas (GHG) emissions, which is predicted to increase to 17% by 2050 if no changes are adapted [1]. The maritime industry is undergoing a significant transition towards utilization of low- and zero-emission reliable energy sources, and smart integration schemes to comply with the international maritime organization's (IMO) regulations [2]. Hydrogen fuel cells (FCs) and batteries are considered as a solution to achieve zero-emission shipping [3]. Already today, small to medium-sized ships operating over shorter distances and with predictable routes can run purely on electricity from batteries and FCs. However, due to the limited energy density of the batteries, they can function as the main power supply for vessels in short-distance shipping segments [4]. The high-power proton exchange membrane fuel cell unit (PEMFC) is a flexible solution that can support the energy needs of a diverse range of vessels and is being considered for installation on larger ships [1], [5].

FCs and batteries are dc power sources whose nonlinear output voltage is different to that of traditional diesel generators, which is inherently ac. The integration of such dc sources together is a challenge that can be met by utilizing several integration schemes [1], [5]. dc distribution systems consisting of a network interconnection of power electronics (PEs) are becoming increasingly common for FC and battery-powered vessels. dc distribution power systems offer several advantages, including increased power interface flexibility through the feedback control, increased efficiency due to the reduced number of required power conversion stages, and the capability to meet various control objectives.

On the downside, PE-based dc power distribution systems have low inertia, which causes challenges in maintaining stability and mitigating oscillations [6]–[8]. The potential stability degradation is more significant when converters are connected to a common dc switchboard [6]. This is due to the interactions among the feedback loops of the interconnected converters. Another stability-related challenge is caused by the constant power load (CPL) behaviour of the tightly regulated high-power drives, which will cause decreases in the stability margin or even system-wide destabilization [9].

In such shipboard hybrid power system (HPS), the system dynamics are changed instantaneously by the interaction of the system dynamics and the control system parameters including governor and converter control which are normally developed by energy management system (EMS), and power management system (PMS). Although each subsystem is independently designed to be standalone stable, the subsystem interactions may substantially alter the control bandwidth from the standalone case. Both issues may compromise control stability at the system-level, and require detailed system-level stability studies during an early design phase.

Several approaches for determining the HPS stability exist. Impedance-based stability has been used in [8], [10] to analyze

Corresponding author: Mehdi Zadeh.

N. Shakeri, M. Zadeh, and A. J. Sørensen are with the Department of Marine Technology, Norwegian University of Science and Technology (NTNU), 7050 Trondheim, Norway (e-mails: nastaran.shakeri@ntnu.no; mehdi.zadeh@ntnu.no; asgeir.sorensen@ntnu.no).

W. Chen is with School of Mechanical and Aerospace Engineering, Nanyang Technological University, Singapore and ABB Pte. Ltd, Singapore (e-mail: wenjie003@e.ntu.edu.sg).

A. Abdelhakim is with the Surface Division, Epiroc Rock Drills AB, 70191 Örebro, Sweden (email: ahmed.abdelhakim@ieee.org).

K. Tai is with School of Mechanical and Aerospace Engineering, Nanyang Technological University, Singapore (e-mail: mktai@ntu.edu.sg).

the source-load interactions based on the component parameters. According to the DNV class rules (DNV-RP-0043) [11], the power system stability is more focused on the system frequency stability because inertia is needed in the traditional ac power system to counteract grid frequency fluctuations. However, in dc power system, especially for the FC and battery hybrid power network, no frequency fluctuations exists. The system stability study turns towards the dc voltage in dc power distribution HPS. The voltage stability in marine systems against CPL for the design stage assessment is studied in [12], [13], and the impact of design parameters on the HPS stability is evaluated in [14]. These works highlight the suitability of the stability analysis with small perturbations and eigenvalue analysis of the state-space matrix to assess the stability of ships and discuss how to predict if a system is either stable or unstable. However, the eigenvalues need to be calculated repetitively with varying the control parameters. It is difficult to identify the specific parameter that contributes most to the system instability, in particular for a high-dimension system. The modal analysis method is an efficient tool to identify the physical nature of modes and measure the coupling between the states of a dynamical system and its modes (eigenvalues) [15]. In terms of eigenvalue sensitivities, participation factors (PFs) represent the sensitivity of an eigenvalue to variations of an element of the state matrix. Sensitivity analysis predicts the movement of the modes and reduces the modes computation burden, especially in a large-scale power system. Thus, it provides an efficient tool during the design of control systems and has wide applications in power system modeling and stability analysis. The authors in [7], [16] perform the sensitivity analysis with respect to the parameter's variation of the power-sharing controllers to tune the control parameters, which are applied on an islanded microgrid, and on an electric aircraft respectively.

Due to the FC's lack of inertia compared to the combustion engines, a delay exists between the adjustment of the load current and the fuel flow rates [17], [18]. The mass balance dynamic in FC refers to the enough fuel/air be present in pipelines to sustain the reaction, which depends on the injected fuel/air flow rate and the fuel/air consumption [19]. Such a dynamic response may lead the FC current to exceed the fuel/air flow rate during the fast load transients, resulting to the fuel starvation phenomena. The combination of the control and monitoring system (i.e., PMS), fuel supply system (governor), thermal management, water management, and power conditioning systems, is often referred to the balance of plant (BoP). The governor ensures that enough fuel and air are available to sustain the reaction under the load variations. The output electric characteristics such as voltage and current depend on the the injected fuel/air, hence, for a stable BoP, FC's governor should be considered in the stability analysis. In this work, the electrical and electrochemical interactive dynamics of the FC system have been analyzed within considering FC governor.

So far, there are few published reports dealing with comprehensive modal analysis using eigenvalue sensitivity and PF for the HPS, especially for the potential FC and battery-fed vessels with highly dynamic and case-dependant marine load profiles. A systematic analysis and design framework are required to ensure HPS stability, and desired performance.

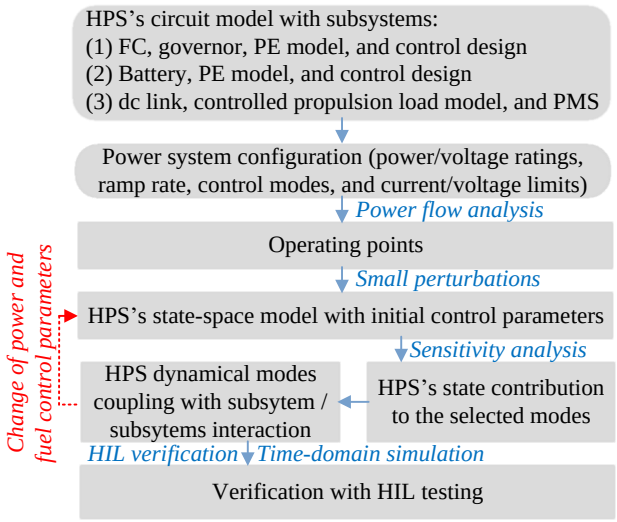

Fig. 1. The methodology flowchart depicting the research framework.

In this work the modal analysis of a large scale FC-powered marine PE-based system is done to assess the system stability under small perturbations. Fig. 1 presents the flowchart depicting the methodology employed in this study. The HPS's circuit model includes FC, battery and load subsystem [19]. The FC subsystem includes the mass balance dynamics, FC's fuel supply system (governor), and different control strategies for the FC converter control. Sensitivity analysis allows the investigation of how the parameters of the state variables are coupled with the system modes (eigenvalues), with the separation of modes into groups based on HPS sources and the propulsion load through a full state-space model. Then, the impact of operating points, control parameters of the governor and converter controllers on the HPS stability is investigated. This allows the influences on poorly damped modes to be explored and to devise a stability enhancement to push the limits and expand the stable operating region of the HPS. The time-domain hybrid shipboard power plant is modelled to verify the control parameters design for the governor and converter control. In addition, a hardware-in-the-loop (HIL) simulator is set up to verify the system's permanence by introducing the communication delay and to perform discrete real-time running states, and validates the HPS model against dynamic ship load profile. The main contributions of this study are listed as follows:

- A modal analysis is conducted which indicates how the parameters of the HPS affect the system modes. The system modes are grouped based on the considered HPS sub-models, particularly FC, battery, and propulsion load. Then the dynamic interactions between sub-models are investigated to find the relative contribution of a system's state to a selected mode. The modal analysis is a systematic and efficient approach applicable to large-scale PE-based power systems. A strong coupling between the subsystems' current state variables and the dc bus volt-

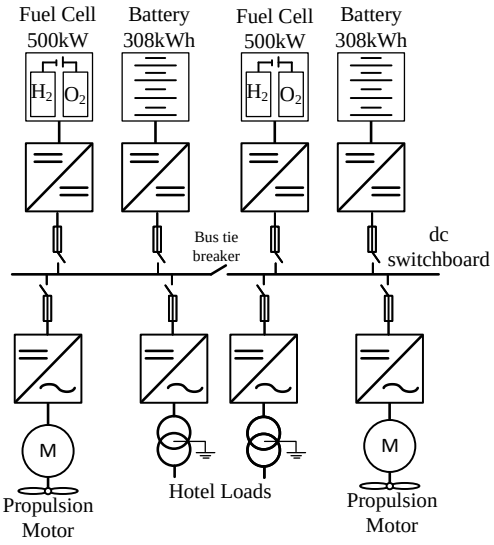

Fig. 2. Single line diagram (SLD) of the shipboard dc hybrid power system in this study, in which the output powers of both fuel cells and batteries are controlled by the dc-dc converters.

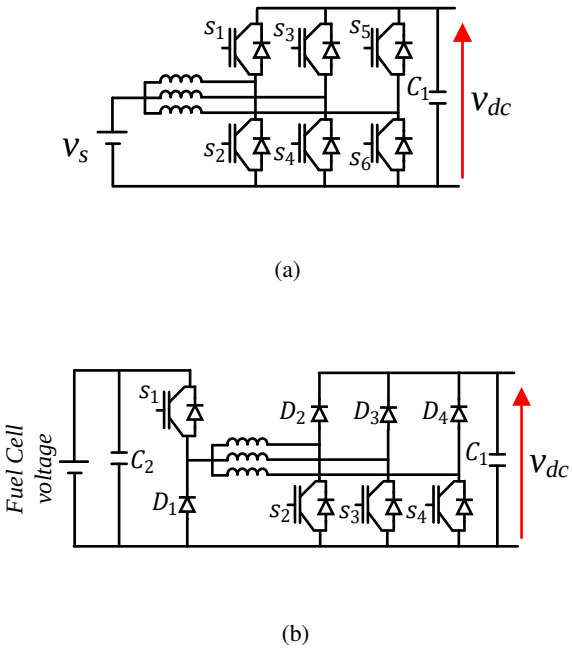

Fig. 3. (a) The full-bridge bidirectional dc-dc converter topology, and (b) back-to-back connected unidirectional buck-boost converter topology.

age dynamics, and also between the governor dynamics and the FC current state are observed. Their controllers therefore need coordination.

- The system coupling with the control parameters' variation is presented in an illustrative form, which in turn simplifies the choice of control parameters. This approach results in reduced computational burden as repetitive calculation of eigenvalues is not needed. By employing modal analysis, a notable impact of the proportional gain of the voltage control loop on the system stability is observed.
- The HPS's analytical model includes the interactive electrical and electrochemical dynamics of the FC, governor, and PEs. Hence, the impact of the FC governor and converter control parameters under different control strategies are investigated, providing valuable insights into the expected FC dynamic interactions in HPS.

The rest of the article is organized as follows. Section II outlines the HPS model, including the subsystems, associated controllers, and the load-sharing strategy. The state-space model based on subsystems is developed in Section III. In Section IV, the stability analysis and eigenvalue sensitivity are successfully applied for the controller tuning, and the performance comparison with the time-domain simulation results is performed in Section V. Section VI evaluates the system plant model in an HIL setup, where the validation tests are performed as well. Finally, conclusion are drawn in Section VII.

II. Dynamic Properties and Modeling of the Fuel Cell-Based Onboard Hybrid Power System (HPS)

A possible, simplified architecture of a typical electrical distribution system for a vessel with FC and battery is illustrated in Fig. 2. According to the class rules, the shipboard power plant distribution is usually redundant to avoid single-point failure. If there is any loss of power on either side of the HPS, the bus-tie will be closed, and the live power sources can feed the propulsion and hotel loads on both the port and starboard sides. Each side of the dc distribution system supplies the propulsion motor and hotel loads with a FC and a battery which are integrated into the main dc switchboard via dc-dc converters. These converters are used for dc voltage level shifting and voltage regulation, power flow control, isolation, and protection. Propulsion and hotel loads are commonly fed through the two-level voltage source inverters (VSIs), used as dc-ac converters. All parts of the HPS are briefly described below. In order to analyze the dynamic interactions, reasonable simplifications are made to the complex system model.

A. dc-dc Converter Model

A dc-dc converter is a two-way PEs unit set up between the dc power/energy sources and the dc bus. The dc-dc converter uses two operation modes referred to as buck and boost. The buck mode is used when energy is transferred from the higher voltage level to the lower one, e.g. charging the battery, while the boost mode is used when energy is transferred from the lower to the higher voltage level. The full-bridge bidirectional dc-dc converter topology is illustrated in Fig. 3(a). A Back-to-back connected buck and boost dc-dc converter can also be used for FC applications [20]. One converter phase is sufficient in buck mode at low FC loading, while three interleaved phases are utilized in boost mode at high FC loading. The latter converter topology is illustrated in Fig. 3(b). The switching frequency of the dc/dc converter is generally 4-5kHz.

There are two methods to model the PE converters, switching detailed models and dynamic average models. The latter is often based on the assumption of the piecewise-linear waveforms of the circuit variables. Detailed switching models consider the impact of parasitic elements, that introduces waveform nonlinearity and complicates the model derivation, that makes them too slow for analysis of rather large power electronic-based systems [21]. Dynamic averaging methods may be used to make the simulation faster when exact switching behavior is not required. However, limitations of the dynamic average model is that although it can correctly predict dc and low frequency behaviour of pulse width modulation (PWM) converters, at high frequencies, it is unable to capture the dynamics of the converter.

Here, the focus of the system-level modeling and stability analysis is to investigate the interactions of the low-level controllers with the HPS subsystems under different control scenarios with the small perturbations. Therefore, the high-frequency switching behavior of the dc-dc converters is neglected, and the converters are modelled based on the average instead of the switching detailed model. Averaging and linearization are the most common approach for modelling and analysis of switching PEs converters in dc shipboard power systems. In several studies the good dynamic and steady-state behavior of averaging methods have been compared with the detailed switching models, validating their effectiveness for system-level studies [21], [22]. The resulting average models are valid for frequencies of up to around half of the switching frequency [22], which is 1-2 kHZ on high power ratings marine applications. The low-frequency variations in the converter's duty cycle induce low-frequency variations in the converter voltages and currents. In this case, the system dynamics are formed mainly by linear dynamics, and hence, the eigenvalues can be used safely for stability analysis. Hence, the average model is selected to configure the HPS here, which is shown in Fig. 4, where d_{fc} and d_{Batt} are the dc-dc converter duty cycles for Fc and battery (saturated between 0 and 1). This model can be used as unified model for both buck and boost mode, where $d_{\mathrm{fc}} = d_{\mathrm{buck}} = 1 - d_{\mathrm{boost}}$.

The dc-dc converter is operated either with voltage or current control, illustrated in Fig. 5. The control of the dc-dc converter is mostly done by the proportional-integral (PI) controllers with k_{p} and k_{i} as the proportional and integral gains. In this work, the fixed dc bus voltage level set-point is implemented to maintain the dc bus voltage constant. A fixed dc bus voltage in HPS refers to a constant voltage level with an allowable continuous voltage variation, i.e., +/-10% of the rating dc bus voltage. Such dc bus voltage range is maintained throughout the HPS for powering the propulsion loads [10], [23]. The converter control scheme in Fig. 5(a) is voltage mode control to ensure the dc bus voltage stability and to maintain the fixed dc bus voltage level. This control scheme contains a dual control loop with the inner current control loop, and the outer voltage control loop. The inner controller's parameters are sufficiently large positive constants to ensure that the inner current loop responds faster than the outer voltage loop. The regulated dc bus voltage level is required to keep the power system stability and persistent load supply, which is the input

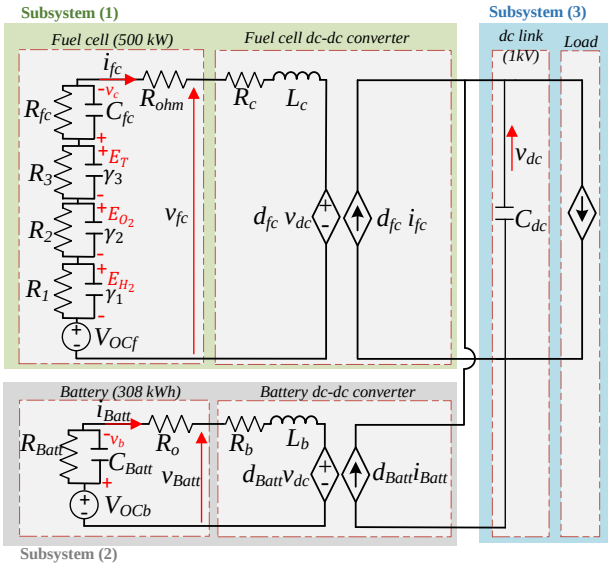

Fig. 4. Schematic of the shipboard dc power system in this study.

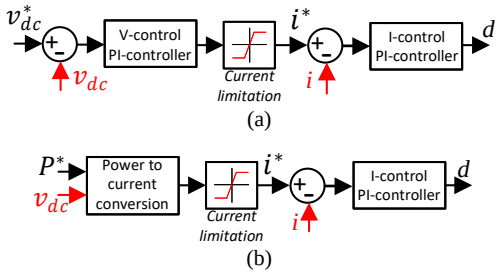

Fig. 5. dc-dc converter (a) voltage mode, and (b) current mode control schemes. Note that measured signals are shown in red, and black signals illustrate the control signals.

signal to the voltage control loop as v_{dc}^{*}. The converter current mode control with a single current control loop is shown in Fig. 5(b), where the current reference is given by the quotient of reference power and dc voltage. The reference power is generated by PMS.

B. Fuel Cell System Model

1) Fuel cell model: The commonly used FC models include detailed electrochemical models, analytical models, empirical models, and electric equivalent circuit (EEC) models. The well-known empirical model introduced in [24] features the FC dynamics at the component-level, under a variety of operating conditions. However, the electrochemical dynamics including mass balance and energy balance dynamics under load transients are not addressed. The real-time model introduced in [25] described the FC voltage while considering the electrochemical dynamics, which is more suitable for component-level integration studies, such as FC's cold start issue. From

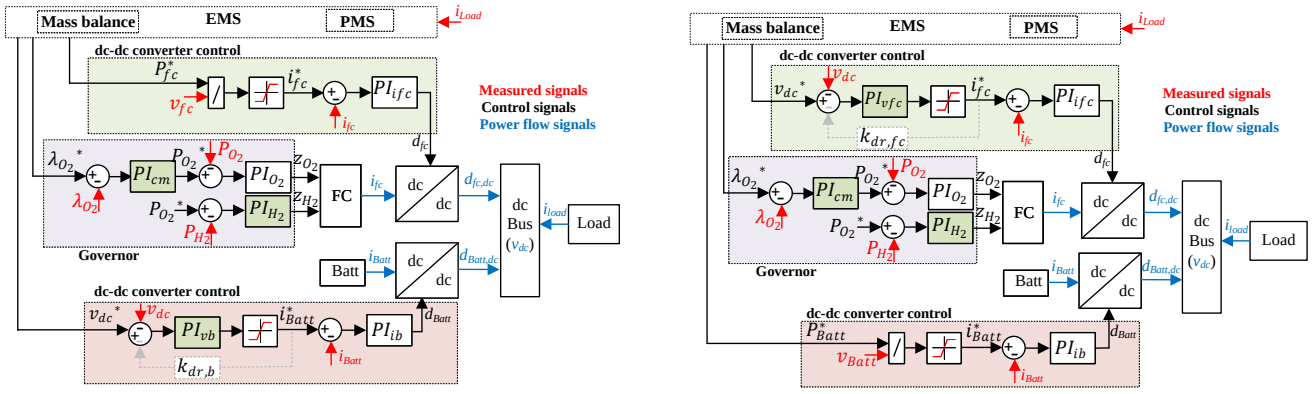

Fig. 6. Control scheme of the FC-powered vessel in this study. Note that the PI controllers in the green block will be evaluated further with stability analysis and time-domain simulations. (a) Scenario I: FC in current mode control and the battery in voltage mode control, and (b) scenario II: FC in voltage mode control and the battery in current mode control. Note that the dashed line in dc-dc converter control boxes illustrates the voltage droop control for FC with the droop rate $k_{dr,fc}$ and the battery with droop rate $k_{dr,b}$.

an electrical system integration perspective, the FC voltage is one of the key operating parameters to consider in HPS design. To that end, the system-level model of FC has been addressed in the literature with various model fidelity levels [20], [26], [27]. The FC dynamics in HPS with a focus on the electrical properties are investigated in [20], [27]. Here, the EEC model is used to represent the FC behaviour which was developed and validated against 500 kW rating FC designed for marine power systems in [19]. The EEC model was obtained based on an integrated electric circuit model which couples the mass balance, energy balance, and electrical properties of FC in a single electrical domain as the forth-order FC circuit model, as is shown in Fig. 4. The analytical expression of the model is described as below.

$$v_{\rm fc} = V_{\rm OCf} + E_{H_2} + E_{O_2} + E_{\rm T} - v_{\rm c} - R_{\rm ohm} i_{\rm fc}, \quad (1)$$

$$\dot{i}_{\rm fc} = \frac{1}{L_{\rm fc}} \left(v_{\rm fc} - R_{\rm c} i_{\rm fc} - d_{\rm fc} v_{\rm dc} \right), \quad (2)$$

$$\dot{v}_{\rm c} = \frac{1}{C_{\rm fc}} i_{\rm fc} - \frac{1}{R_{\rm fc} C_{\rm fc}} v_{\rm c}, \quad (3)$$

$$\dot{E}_{H_2} = \frac{1}{\gamma_1} i_{\rm fc} - \frac{1}{R_1 \gamma_1} E_{H_2}, \quad (4)$$

$$\dot{E}_{O_2} = \frac{1}{\gamma_2} i_{\rm fc} - \frac{1}{R_2 \gamma_2} E_{O_2}, \quad (5)$$

$$\dot{E}_{\rm T} = \frac{1}{\gamma_3} i_{\rm fc} - \frac{1}{R_3 \gamma_3} E_{\rm T}, \quad (6)$$

where $v_{\rm fc}$ is the FC terminal voltage, $V_{\rm OCf}$ is the open-circuit voltage, E_{H_2} and E_{O_2} represent the mass balance dynamics as a function of FC fuel flow rates, and partial pressures, which are described as RC circuits by $R_1\gamma_1$, and $R_2\gamma_2$, $E_{\rm T}$ describes the energy balance dynamic as a function of FC temperature described as an RC circuit by $R_3\gamma_3$, $v_{\rm c}$ is the transient voltage through the parallel $R_{\rm fc}C_{\rm fc}$ circuit, depicting that FC voltage varies exponentially with the time constant $\tau_{\rm fc} = R_{\rm fc}C_{\rm fc}$, which is around 0.1-0.2s, $R_{\rm ohm}$ is the resistor, $i_{\rm fc}$ is the FC current, which is equal to the current passed through the inductance of the converter, $L_{\rm C}$ and $R_{\rm C}$ are the FC dc-dc converter inductance and resistor, $v_{\rm dc}$ is the dc link voltage, and finally, $d_{\rm fc}$ is the FC dc-dc converter duty cycle.

Here, it is briefly explained how E_{H_2}, E_{O_2}, and $E_{\rm T}$ are developed as $R_i\gamma_i$ circuits, where $i \in 1, 2, 3$. Here, R_i and γ_i are the RC circuits' resistor and capacitor respectively. Generally, the transient voltage drop of the ith circuit (E_i) in response to the FC current change (ΔI) is shown in (7), which can be written in Laplace domain as (8), where k_i refers to $\frac{1}{\gamma_i}$, and τ_i is the $R_i\gamma_i$ circuit's time constant. This time constant of a first-order LTI system (τ_i) in response to a step current input ΔI is the time needed by the voltage responses to decay to 37% of its initial value [28]. This shows the correlation between transient voltage drop E_i and the system dynamic time response τ_i. The voltage drop is happening in which step the current steps up simultaneously to some value because of the voltage drops across the resistor and mass balance and energy balance dynamics in EEC and reaches its steady-state value by a time delay due to the capacitance $\tau_{\rm RC}$, hydrogen flow rate τ_{H_2}, and oxygen flow rate τ_{O_2}. This study considers that the periods of the τ_{H_2} and τ_{O_2} are approximately three and six times that of the RC circuit $\tau_{\rm RC}$, i.e., $\tau_{\rm RC}$ is 0.11s, τ_{H_2} is 0.337s, and τ_{O_2} is 0.647s. More parameter's details can be found in [19]. This developed FC model has to have a continuous supply of reactants (fuel/air flow rates) adjusted by the current drawn from the FC stack. This is possible with the design of a governor on both hydrogen and oxygen systems.

$$E_{\rm RC,i}(t) = \overbrace{\Delta I \cdot R_{\rm i}}^{E_{\rm i}} (1 - e^{\frac{-t}{\tau_{\rm i}}}) = E_{\rm i}(1 - e^{\frac{-t}{\tau_{\rm i}}}), \quad (7)$$

$$E_{\rm RC,i}(s) = \frac{K_{\rm i}}{s + \tau_{\rm i}} \frac{\Delta I}{s}. \quad (8)$$

2) Fuel cell governor: Power generation in FCs relies on the continuous supply of oxygen (O_2) and hydrogen (H_2).

The governor block shown in Fig. 6 includes two subsystems: H_2 and the air subsystems. Generally, an increase in the FC current i_{fc} causes a decrease in pressures, which makes the governor to regulate fuel/air flow rates to stabilize pressures through actuators, whose performance setting time is 10-90% of 50ms for H_2 and 20ms for O_2 supply system [29]. The actual extent of this delay depends on the sizing of the manifolds and the rate of fuel consumption. To meet this performance, the H_2 pressure controller must be almost between two and three times faster than the O_2 side, meaning that hydrogen partial pressure (P_{H_2}) follows hydrogen partial pressure (P_{O_2}).

The problem of FC fuel/air starvation and control has been extensively studied in [18], [29]. In this paper, the electric load is effectively controllable by the power conditioning unit, whose impacts on the system pressures will be compensated by the mass balance block shown in Fig. 6. At the steady-state, the FC current change must be followed by a corresponding change in the fuel/air flow rate. Hence, the governor is developed in a flow-controlled design with a closed-loop operation, where fuel/air flow rates are changed according to the FC current changes. Reasonable simplifications are made to the complex governor for the purpose of the system-level stability analysis. According to the ideal gas law and the mole conservation rule, the partial pressure of each gas is balanced by the gas inlet flow rate minus the gas consumption and the gas outlet flow rate. The hydrogen partial pressure derivative is given as follows

$$\dot{P}_{H_2} = \frac{R_{\text{u}}T}{V_{\text{a}}}(\overbrace{M_{H_{2,\text{in}}} - M_{H_{2,\text{out}}}}^{M_{H_{2,\text{net}}}} - \frac{NA_{\text{fc}}i_{\text{fc}}}{2F}), \tag{9}$$

where the detailed explanation of parameters can be found in [17]. $M_{H_{2,\text{in}}}$ and $M_{H_{2,\text{out}}}$ are the inlet and outlet mole flow rate of hydrogen (mol/sec), which can convert to the mass flow rate (kg/sec) by using the molar mass of hydrogen (2.0158 gr/mol). For simplicity, it is defined that

$$C_{H_2} = \frac{NA_{\text{fc}}}{2F}. \tag{10}$$

In steady-state, the net mass flow rate $M_{H_{2,\text{net}}}$ is equal to the usage of hydrogen, which should be regulated through the governor under transients, with z_{H_2} (pu) as the fuel index. Therefore, the H_2 governor can be represented through

$$\dot{P}_{H_2} = \frac{R_{\text{u}}T}{V_{\text{a}}}(-C_{H_2}i_{\text{fc}} + z_{H_2}), \tag{11}$$

$$z_{H_2} = k_{p,H_2}\left(P^*_{H_2} - P_{H_2}\right) + k_{i,H_2}X_u, \tag{12}$$

$$\dot{X}_u = P^*_{H_2} - P_{H_2}, \tag{13}$$

where z_{H_2} is determined by a PI controller (PI_{H_2}) with k_{p,H_2} and k_{i,H_2}, and X_u is the auxiliary state variable describing pressure error dynamics for the control loop, shown in Fig. 6.

Another governor subsystem is responsible for delivering the air (including about 21% oxygen). Injection of the oxygen with the air molar mass of 28.85 gr/mol includes two control loops as shown by Fig. 7; the inner loop control for stabilizing P_{O_2}, and the outer control loop to regulate the oxygen excess ratio λ_{O_2} which is defined as the ratio of the oxygen supplied

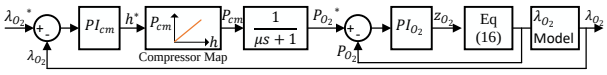

Fig. 7. Oxygen governor with the $\lambda^*_{O_2}$ generated from mass balance block and the simplified compressor model.

and the oxygen consumed [17]. Therefore, the main control objective here is to force λ_{O_2} to track $\lambda^*_{O_2}$, generating from mass balance block that lies between 2 and 2.5 [18]. Within this range, the maximized net power is achieved, which is considered constant at 2 in this work. The oxygen partial pressure derivative is given as the following equation as Cathode model conservation equation [17]:

$$\dot{P}_{O_2} = \frac{R_{\text{u}}T}{V_{\text{c}}}(\overbrace{M_{O_{2,\text{in}}} - M_{O_{2,\text{out}}}}^{M_{O_{2,\text{net}}}} - \frac{NA_{\text{fc}}i_{\text{fc}}}{4F}). \tag{14}$$

The thermodynamic parameters used in (9-14) are listed in the following. $R_{\text{u}} = 8.31[J/mol.K]$ is the ideal gas constant, $v_{\text{a}} = 0.005[m^3]$ is the anode volume, $v_{\text{c}} = 0.02[m^3]$ is the cathode volume, $T = 318[K]$ is the FC temperature, $F = 964873[C/mol]$ is Faraday constant, $N = 60$ is number of cells, and $A_{\text{fc}} = 60[cm^2]$ is the cell's active area. For simplicity, it is defined that

$$C_{O_2} = \frac{NA_{\text{fc}}}{4F}. \tag{15}$$

In steady-state the net mass flow rate $M_{O_{2,net}}$ is equal to the usage of oxygen, which should be regulated through the governor under transients, with z_{O_2} (pu) as the oxygen index. Therefore, the O_2 governor can be represented as

$$\dot{P}_{O_2} = \frac{R_{\text{u}}T}{V_{\text{c}}}(-C_{O_2}i_{\text{fc}} + z_{O_2}), \tag{16}$$

$$z_{O_2} = k_{p,O_2}\left(P^*_{O_2} - P_{O_2}\right) + k_{i,O_2}X_{O_2}, \tag{17}$$

$$\dot{X}_{O_2} = P^*_{O_2} - P_{O_2}, \tag{18}$$

where z_{O_2} is determined by a PI controller (PI_{O_2}) with k_{p,O_2} and k_{i,O_2}, and X_{O_2} is the auxiliary state variable describing pressure error dynamics. For simplicity and to avoid dynamics of torque and compressor model, the compressor map model is used to generate the partial pressure reference ($P^*_{O_2}$) for the inner control loop. That is done by considering the supply manifold model as a linear first-order filter model as $\frac{1}{\mu s+1}$ with $\mu = 0.33$. The compressor map is defined based on the compressor pressure P_{cm} and the desired compressor mass flow rate h^* as

$$h^* = k_{\text{p,cm}}\left(\lambda^*_{O_2} - \lambda_{O_2}\right) + k_{\text{i,cm}}X_\lambda, \tag{19}$$

$$\dot{X}_\lambda = \lambda^*_{O_2} - \lambda_{O_2}, \tag{20}$$

where $k_{\text{p, cm}}$ and $k_{\text{i, cm}}$ are the outer loop PI controller (PI_{cm}) parameters, X_λ is the auxiliary state variable describing oxygen access ratio error dynamics.

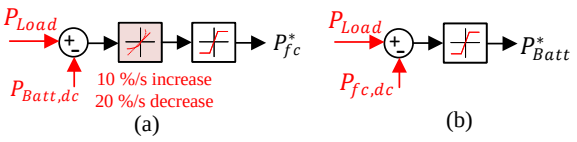

Fig. 8. PMS design to generate: (a) the FC power setpoint P^*_{fc} in scenario I, and (b) the battery power setpoint P^*_{Batt} in scenario II.

3) Fuel cell dc-dc converter: Based on the control scenarios shown in Fig. 6, d_{fc} can be obtained to regulate the FC output voltage/power. In Fig. 6(b), during scenario II, the FC' converter with a dual control loop including the inner current control loop (PI_{ifc}) and the outer voltage control loop (PI_{vfc}) ensures the dc bus voltage v_{dc} stability. Here, d_{fc} is given by

$$d_{\text{fc}} = k_{\text{pi,fc}}\left(i_{\text{fc}} - i^*_{\text{fc}}\right) + k_{\text{ii,fc}} X_{\text{fc,i}}, \tag{21}$$

$$\dot{X}_{\text{fc,i}} = i_{\text{fc}} - i^*_{\text{fc}}, \tag{22}$$

$$i^*_{\text{fc}} = k_{\text{pv,fc}}\left(v^*_{\text{dc}} - v_{\text{dc}}\right) + k_{\text{iv,fc}} X_{\text{fc,v}}, \tag{23}$$

$$\dot{X}_{\text{fc,v}} = v^*_{\text{dc}} - v_{\text{dc}}, \tag{24}$$

$$\tau_{\text{fc,r}} = \frac{T_{20\%-100\%}}{80\%}\ , r_{\text{fc}} = \frac{\Delta P_{\text{fc}}}{\tau_{\text{fc,r}}}, \tag{25}$$

where $X_{\text{fc,v}}$ is the auxiliary state variable described the voltage error dynamics for the outer voltage control loop of the dc-dc converter with a PI controller (PI_{vfc}) with $k_{\text{pv,fc}}$ and $k_{\text{iv,fc}}$ to generate the FC current reference i^*_{fc} for the inner current control loop. The regulated dc voltage level is the input signal to the voltage control loop as v^*_{dc}. In (25), the FC ramp rate r_{fc} is defined as the max rate of the FC power change ΔP_{fc}, which is deduced from the dynamic of the FC and its auxiliaries [20]. In this work, is assumed that the FC power can be ramped up from 20% to 100% of the rated power within 1s (20kW/s-%10/s). To meet the requirements for the rate of power change allowed by the FC system as the ramp rate r_{fc}, the time constant $\tau_{\text{fc,r}}$ should be considered while tuning PI_{vfc} parameters to generate i^*_{fc}, with a non-negative current limit set according to the max value allowed by the FC system. $X_{\text{fc,i}}$ is the auxiliary state variable described current error dynamics for the inner current control loop of the dc–dc converter with a PI controller (PI_{ifc}) with $k_{\text{pi,fc}}$ and $k_{\text{ii,fc}}$ to calculate the duty cycle d_{fc}, i_{fc} is the measured FC current, which is non-negative. The inner PI controller parameters are sufficiently large positive constants to ensure that the inner current loop responds faster than the outer voltage loop.

In Fig. 6(a), during scenario I, FC is in current mode control with the current control loop (PI_{ifc}), while the battery with higher power density ensures the dc bus voltage stability. Here to generate the current reference i^*_{fc} for the current control loop, the power reference P^*_{fc} is calculated according to the FC ramp rate limit from PMS, as shown in Fig. 8(a), where $P_{\text{Batt,dc}}$ is the battery power delivered to the dc bus. So, d_{fc} in scenario I is calculated by (21) and (22).

It is possible to drive a state-space model of the FC system including converter control and governor From (1-25), where the state vector is $X_{\text{fc,I}} = [i_{\text{fc}}\ E_{H_2}\ E_{O_2}\ E_{\text{T}}\ v_{\text{c}}\ X_{\text{fc,i}}\ P_{H_2}\ X_{\text{u}}\ P_{O_2}\ X_{O_2}\ X_{\lambda}]^T_{11\times 1}$ for the control scenario I, and $X_{\text{fc,II}} = [i_{\text{fc}}\ E_{H_2}\ E_{O_2}\ E_{\text{T}}\ v_{\text{c}}\ X_{\text{fc,i}}\ X_{\text{fc,v}}\ P_{H_2}\ X_{\text{u}}\ P_{O_2}\ X_{O_2}\ X_{\lambda}]^T_{12\times 1}$ for the control scenario II to describe the completed FC system model.

C. Battery and dc-dc Converter Model

First-order Thevenin circuit model of the Li-ion battery has been used to determine the dynamic characteristics of the battery [30], including a series resistor R_{o} and an $R_{\text{Batt}}C_{\text{Batt}}$ parallel network to predict the battery response to transient load events at a particular state of charge (SOC), which is shown in Fig. 4. While unloaded, the battery module delivers a specific voltage, the so-called open-circuit voltage V_{OCb}, which varies with SOC. This correlation is an important parameter for calculating the SOC during operation. However, in the developed HPS, the battery modules address the high-frequency component, which means it is likely that SOC can change rapidly (i.e., as power-type cells). Therefore, it is considered that V_{OCb} is constant, and the self-discharging resistance is ignored in this work.

The battery exchanges energy with the dc power system through the corresponding bidirectional dc-dc converter, which regulates the output voltage and power flow. The same averaged switch model as a unified model for buck and boost mode is used for the battery dc-dc converter shown in Fig. 4. Therefore, the resulting battery model becomes as follows

$$\dot{i}_{\text{Batt}} = \frac{1}{L_{\text{b}}}\left(V_{\text{OCb}} - v_{\text{b}} - R_{\text{o}} i_{\text{Batt}} - R_{\text{b}} i_{\text{Batt}} - d_{\text{Batt}} v_{\text{dc}}\right), \tag{26}$$

$$\dot{v}_{\text{b}} = \frac{1}{C_{\text{Batt}}} i_{\text{Batt}} - \frac{1}{R_{\text{Batt}} C_{\text{Batt}}} v_{\text{b}}, \tag{27}$$

$$SOC = SOC\,(0) - \frac{1}{K_{\text{b}} Q_{\text{b}}} i_{\text{Batt}}, \tag{28}$$

$$d_{\text{Batt}} = k_{\text{pi,b}}\left(i_{\text{Batt}} - i^*_{\text{Batt}}\right) + k_{\text{ii,b}} X_{\text{b,i}}, \tag{29}$$

$$\dot{X}_{\text{b,i}} = i_{\text{Batt}} - i^*_{\text{Batt}}, \tag{30}$$

$$i^*_{\text{Batt}} = k_{\text{pv,b}}\left(v^*_{\text{dc}} - v_{\text{dc}}\right) + k_{\text{iv,b}} X_{\text{b,v}}, \tag{31}$$

$$\dot{X}_{\text{b,v}} = v^*_{\text{dc}} - v_{\text{dc}}, \tag{32}$$

where i_{Batt} is the battery current which its direction changes based on if the battery is in charge or discharge mode. v_{b} is the transient voltage in the battery through the capacitor C_{Batt}, R_{b} and L_{b} are the battery dc-dc converter resistor and inductance, v_{dc} is the measured voltage of dc bus, d_{Batt} is the battery dc-dc converter duty cycle (saturated between 0 and 1). Depending on the control mode of the battery converter d_{Batt} can be arranged. In scenario I, it is controlled through dual control loops, outer voltage loop and inner current loop. In this case, d_{Batt} is generated by (29-32), where $X_{\text{b,v}}$ is the auxiliary state variable described the voltage error dynamics for the outer voltage control loop with a PI controller (PI_{vb}) with the tuning parameters $k_{\text{pv,b}}$ and $k_{\text{iv,b}}$ to generate i^*_{Batt} as the battery current reference for the inner current loop control which is bounded by a limit defined according to the battery C-rating, $X_{\text{b,i}}$ is the auxiliary state variable described the current

error dynamics for the current control loop with a PI controller (PI_{ib}) with $k_{\text{pi,b}}$ and $k_{\text{ii,b}}$. In scenario II, the battery dc-dc converter is controlled by a current control loop (PI_{ib}) where the power reference P^*_{Batt} is defined based on the PMS design (Fig. 8(b)), and d_{Batt} is generated by (29) and (30). Finally, the battery output current i_{Batt} is integrated over time to derive the change of the battery SOC from its initial charge $SOC\,(0)$ with a conversion factor of K_{b}, and the rated capacity of the battery Q_{b}. The rate of change in SOC is proportional to the i_{Batt}, which is bounded by putting a limit on i^*_{Batt}, defined according to the battery C-rating.

It is possible to drive the state-space model of the battery system, including the converter control in view of (26)-(32), where the state vector is $X_{\text{Batt,I}} = [i_{\text{Batt}}\ v_{\text{b}}\ X_{\text{b,i}}\ X_{\text{b,v}}\ SOC]^T_{5\times 1}$ for the scenario I, and $X_{\text{Batt,II}} = [i_{\text{Batt}}\ v_{\text{b}}\ X_{\text{b,i}}\ SOC]^T_{4\times 1}$ for the scenario II to describe the completed battery system model.

D. Propulsion Load and dc Bus Model

As the load model is not the focus of this paper, the HPS feeding an ideal constant power load (CPLs) is studied here, where propulsion motors and other onboard hotel loads are connected to the dc switchboard through a specific power converter, which are tightly controlled with its control bandwidth sufficiently high to make the load power independent of the dc-link voltage variations, and rejecting the dc-link voltage disturbances [14]. As the propulsion loads make up the majority of the total load, the auxiliary smaller loads such as hotel loads' oscillations are omitted from considerations [8]. Thus, the propulsion load and ship hotel loads of the vessel are represented with a controllable current source [10], [14], [27].

The dc switchboard integrates all sources and load subsystems through the equivalent capacitor bank C_{dc}, including the individual capacitors in each component, as shown in Fig. 4. The resulting model is presented as

$$\dot{v}_{\text{dc}} = \frac{1}{C_{\text{dc}}}\left(d_{\text{fc}} i_{\text{fc}} + d_{\text{Batt}} i_{\text{Batt}} - i_{\text{load}}\right), \tag{33}$$

$$i_{\text{load}} = \frac{P_{\text{load}}}{v_{\text{dc}}}, \tag{34}$$

where (34) represents the original controlled current source as CPL load, with P_{Load} as load power, which is nonlinear; it is common to linearize it around a dc voltage operating point v_{dco}, and load power operating point P_{CPLo}, which is expressed as follows:

$$i_{\text{CPL}} \approx \frac{P_{\text{CPL}}}{v_{\text{dco}}} - \frac{P_{\text{CPLo}}}{v^2_{\text{dco}}} v_{\text{dc}}, \tag{35}$$

where the instantaneous value of impedance is always positive and the incremental impedance is always negative, which causes the current to increase when the voltage decreases. The current decreases when the voltage increases, and may cause instabilities [16].

E. Power Management System (PMS)

To maintain a stable operation of an autonomous marine system, the total power generation must be effectively controlled and properly dispatched to meet the total power demand of the propulsion loads. In this work, the power control strategy is determined by the difference between the power demand reference and the total power generation, shown in Fig. 8, with the control objectives as follows:

1) The vessel's load power demand P_{load} is satisfied regardless of its dynamical changes.
2) FC ramp rate defined as below is satisfied.

$$r_{\text{fc}} = \begin{cases} -20A/s \le \frac{\mathrm{d}i_{\text{fc}}}{\mathrm{d}t} \le 20A/s, & \text{for ramping up,} \\ -40A/s \le \frac{\mathrm{d}i_{\text{fc}}}{\mathrm{d}t} \le 40A/s, & \text{for ramping down.} \end{cases}$$

The other basic load-sharing mechanism in dc-distributed power network is dc voltage droop control [14], [27]. Basically, with the voltage droop control, all the power sources share the load based on the dc bus voltage. For the energy storage power sources, such as FCs and batteries, the dc voltage droop control is implemented by the dc-dc converters. The dc droop control philosophy is shown in Fig. 6 through the dashed line in the dc-dc converter control boxes by a dual control loop, with $k_{\text{dr,FC}}$ as the FC droop rate, and $k_{\text{dr,b}}$ as the battery droop rate. The current set-points to the current loops control (PI_{ifc} and PI_{ib}) are then produced by the droop as (36) and (37) such that dynamic load changes are handled by the droop gain design, i.e., more droop rate enables to follow the load faster, and less droop rate will cause the power source to take fewer load changes than one with a more droop rate. Usually, the dc voltage droop rate is not larger than 5% [27].

$$i^*_{\text{fc}} = (v^*_{\text{dc}} - v_{\text{dc}} - k_{\text{dr,fc}} i_{\text{fc}})(PI_{\text{vfc}}), \tag{36}$$

$$i^*_{\text{Batt}} = (v^*_{\text{dc}} - v_{\text{dc}} - k_{\text{dr,b}} i_{\text{Batt}})(PI_{\text{vb}}). \tag{37}$$

III. State-Space Model and Sensitivity Analysis of the Shipboard Hybrid Power System

This section discusses the total model of the HPS that has been divided into various subsystems. Firstly, the FC, its governor and dc-dc converter, secondly the battery and its dc-dc converter, and finally the dc bus and propulsion load, as shown in Fig. 4. In the following it is shown how these submodels are merged to form the linearized system matrix.

A. System State-Space Model

The power system model for the voltage stability analysis is formulated as a set of Differential Algebraic Equations (DAEs) as follows:

$$\dot{\boldsymbol{x}} = \boldsymbol{f}(\boldsymbol{x}, \boldsymbol{u}). \tag{40}$$

The linearized system model is derived by linearizing the system near the operating point $(\boldsymbol{x_0}, \boldsymbol{u_0})$ for sufficiently small perturbations as follows:

$$\Delta\dot{\boldsymbol{x}} = \boldsymbol{f}_x \Delta\boldsymbol{x} + \boldsymbol{f}_u \Delta\boldsymbol{u}, \tag{41}$$

where $\Delta\boldsymbol{x} = \boldsymbol{x} - \boldsymbol{x_0}$ and $\Delta\boldsymbol{u} = \boldsymbol{u} - \boldsymbol{u_0}$; f_x and f_u are the Jacobian matrices evaluated at $(\boldsymbol{x_0}, \boldsymbol{u_0})$, i.e, $\frac{\partial f}{\partial x}\,|_{(\boldsymbol{x_0},\boldsymbol{u_0})}$ etc. The operating points can be obtained based on the load flow analysis. Then the resulting linearized DAEs can be put in the following state-space form:

$$\Delta\dot{x} = A\Delta x + B\Delta u, \tag{42}$$

where A is the state matrix and B is the input matrix of the original system given in (40), with the inputs as $u = \left[i^*_{\text{fc}}\ P^*_{O_2}\ \lambda^*_{O_2}\ i^*_{\text{Batt}}\ v^*_{\text{dc}}\ P_{\text{CPL}}\right]^T_{6\times1}$. The submatrices discussed in the last section are combined to form the state-space model of the total system as A_{I} and A_{II} for two different control scenarios shown in Fig. 6. A_{I} and A_{II} determine interactions between the submatrices, including the coupling between the FC subsystem and the load subsystem as $[A_{fc/dc}]$ and $[A_{dc/fc}]$, and the coupling between the battery subsystem and the load subsystem as $[A_{Batt/dc}]$ and $[A_{dc/Batt}]$, demonstrating that the dc bus and load subsystem with the system state Δv_{dc} functions as a bridge between other dc subsystems.

TABLE I
SPECIFICATION OF PARAMETERS OF THE HPS

Battery	Value	PEMFC	Value
Capacity	$308[kWh]$	Rated power	$500[kW]$
V_{Nominal}	$805[V]$	$V_{\text{Operating}}$	$500-1000[V]$
$I_{b,\text{limit}}$	$\pm600[A]$	Current range	$0-1200[A]$
V_{OCb}	$750[V]$	V_{OCf}	$900[V]$
R_{o}	$2[m\Omega]$	R_{fc}	$1.0973[\Omega]$
R_{Batt}	$13[m\Omega]$	C_{fc}	$0.1[F]$
C_{Batt}	$14300[F]$	R_{ohm}	$0.05[\Omega]$
$K_{\text{Batt}}, Q_{\text{Batt}}$	$3600[s], 500[Ah]$	$\gamma_1, \gamma_2, \gamma_3$	$6e^{-}3, 8e^{-}3, 0.15[F]$
SOC	$20-80[\%]$	R_1, R_2, R_3	$3, 11, 13[m\Omega]$
R_b	$0.01[\Omega]$	R_c	$0.01[\Omega]$
L_b	$20[mH]$	L_c	$20[mH]$

B. Sensitivity Analysis

This work focuses on how the parameters of the state variables are coupled with the power system modes (eigenvalues) through the definition of the system's state-space representation. PF analysis provides a useful insight into what features of the HPS give rise to a given mode [15], [31]. It is a measure of the relative participation of the k_{th} state variable in the i_{th} mode, which is computed by the product of the left eigenvectors w_{ki}, and the right eigenvectors v_{ik} as:

$$p_{ki} = \frac{\lambda_i}{a_{ki}} = \frac{|w_{ki}|\,|v_{ik}|}{\sum_{j=1}^{n}|w_{kj}|\,|v_{jk}|}. \tag{43}$$

The participation matrix is a matrix of all the PFs. The higher the PF, the more the k_{th} state participates in determining the i_{th} mode. For simplicity, PFs are normalized based on the highest value.

IV. RESULTS AND DISCUSSION

In practice, the HPS system parameters vary during operation, such as operating conditions and control system parameters. Any such change affects the system eigenvalues. This section deals with a comprehensive modal analysis to estimate the eigenvalue change tendency and allows the influences on poorly damped modes (eigenvalues with the negative real values closer to zero) to be explored to expand the stable operating region of HPS through a change of control parameters.

The eigenvalues are derived from A_{I} and A_{II} to investigate the system stability of the HPS shown in Fig. 4 through the locus of the eigenvalues against HPS operating points and the control parameters. Table I displays the HPS parameters.

1) Impact of operating points: Load power is the main concern when considering HPS operating conditions. Fig. 9(a) shows the eigenvalues distribution and trajectory of the system for A_{I}, with the P_{load} varying from 100kW to 700kW (markers 'x'), where the step size is equal to 100kW. It can be clearly seen that the higher load power deteriorates the system stability as dominant eigenvalue λ_{10} moves toward the right half plane (RHP). When P_{load} is larger than 600kW, λ_{10} crosses the imaginary axis, and the system becomes unstable.

In Fig. 9(b), during scenario II (A_{II}) with a less strict limit on the FC power ramp rate to generate i^*_{fc}, the dominant eigenvalues λ_2 and λ_{14} (markers 'x' and 'o' respectively) approach the RHP when load power is increased with the same step size as Fig. 9(a). From here, the stability assessment will be done on $P_{\text{load}} = 600$kW, which is the most critical operating point for both control scenarios.

The HPS is well-damped during low-load power range, which is very important for marine ship operations. Examples of such seagoing ships are dynamically positioned (DP) vessels in zero-emission mode, where the basic DP functionality is either to keep a fixed position and heading or to move slowly from one location to another [32]. DP vessels are known to spend up to 90% of total energy consumption when operating at partial loads, less than 50–60% of full power, i.e., the average load demand is about 20–30% of the total power capacity for DP ships operating in North sea. The HPS can be designed in a way that the batteries manage load variations such as to support peak-load, or absorb remaining power during low-load, while FCs take the partial load to substitute diesel generators.

2) Identification of mode groups: The behaviour of the modes of the study HPS subsequent to their coupling with subsystems is investigated. The HPS has been divided into various clusters, in particular FC, battery, and dc bus and load,

$$A_{\text{I}} = \begin{bmatrix} [\,A_{fc}\,]_{11\times11} & [\,0\,]_{11\times5} & [\,A_{fc/dc}\,]_{11\times1} \\ [\,0\,]_{5\times11} & [\,A_{Batt}\,]_{5\times5} & [\,A_{Batt/dc}\,]_{5\times1} \\ [\,A_{dc/fc}\,]_{1\times11} & [\,A_{dc/Batt}\,]_{1\times5} & [\,A_{dc}\,]_{1\times1} \end{bmatrix}_{17\times17} \tag{38}$$

$$A_{\text{II}} = \begin{bmatrix} [\,A_{fc}\,]_{12\times12} & [\,0\,]_{12\times4} & [\,A_{fc/dc}\,]_{12\times1} \\ [\,0\,]_{4\times12} & [\,A_{Batt}\,]_{4\times4} & [\,A_{Batt/dc}\,]_{4\times1} \\ [\,A_{dc/fc}\,]_{1\times12} & [\,A_{dc/Batt}\,]_{1\times4} & [\,A_{dc}\,]_{1\times1} \end{bmatrix}_{17\times17} \tag{39}$$

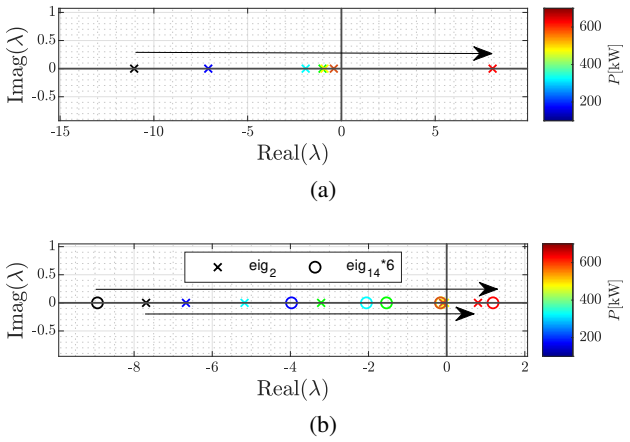

Fig. 9. (a) Eigenvalue 10 (i.e., λ_{10}) movement by increasing the load power from 100kW to 700kW for control scenario I, and (b) eigenvalue 2 (i.e., λ_2) and eigenvalue 14 (i.e., λ_{14}) movements by increasing the load power from 100kW to 700kW for control scenario II. Note that the color code in the bar is used to highlight the eigenvalues for the specific load power value.

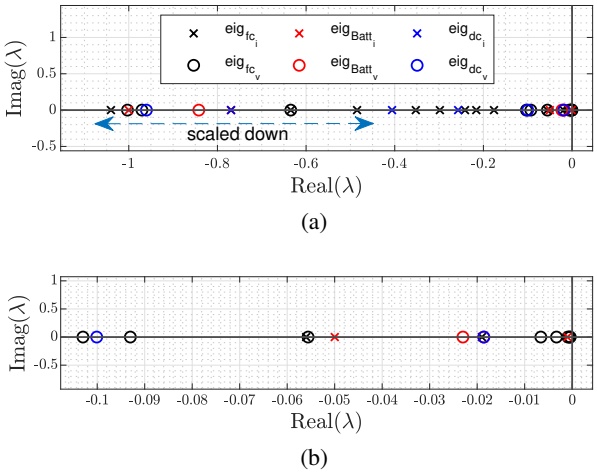

Fig. 10. (a) Locus of eigenvalues of the HPS under study at 600kW load power which are grouped into clusters including eig_{fc}, eig_{Batt} and eig_{dc} showing the cluster of the subsystem as FC, battery and load respectively, (b) less damped modes of the HPS in both scenarios. Note that the index i and v represent the FC control mode as current (scenario I) and voltage mode control (scenario II).

with their power and fuel controllers. Fig. 10 lists the modes of the studied system according to the control scenarios and the clusters' state participation in determining the system's mode. It should mention that modes are grouped based on the relatively highest PF, although coupling exists between the state variables of different clusters for some modes. Fig. 10(b) depicts less damped modes. During scenario II, the system is less damped compared to the scenario I. Therefore, FC as the subsystem that is in voltage mode control deteriorates the system voltage stability. In the following it turns out through the sensitivity analysis that the dc bus voltage is impacted by the state variable parameters related to the voltage control loop.

3) Impact of control parameters: This subsection studies the behaviour of the eigenvalues of the HPS subsequent to a change in controller parameters. Table II lists the sensitivity

TABLE II
SENSITIVITY OF CRITICAL DOMINANT MODES IN SCENARIO I

Mode i	P_{H_2}	P_{O_2}	i_{fc}	i_{Batt}	$X_{\text{b,v}}$	v_{dc}
λ_2	0.9092	0.03	0.03	0	0	0
λ_3	0	0.9699	0.021	0	0	0
λ_5	0.041	0.9703	0.143	0	0	0
λ_{10}	0	0	0.03	0.375	0.384	0.9831
λ_{15}	0	0	0.928	0.32	0.236	0.9022

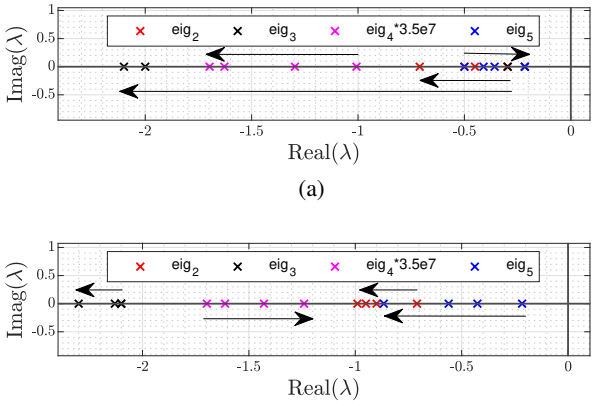

Fig. 11. Eigenvalue movements in scenario I at the operating point of 600kW with respect to varying governor parameters: (a) $k_{\text{p, cm}}$ sweep from 1 to 0.02 with k_{p,H_2} constant at 1.2e1, (b) k_{p,H_2} sweep from 1.2e1 to 2e1 with $k_{\text{p, cm}}$ constant at 0.02, to design the governor.

of less damped modes with the corresponding state variables of A_{I}. The critical modes λ_2, λ_3, and λ_5 are sensitive to the FC's governor state variables (P_{H_2}, P_{O_2}, and i_{fc}). The relevant PFs are displayed within the boxes in Table II. By changing the governor control parameters, i.e., $k_{\text{p,cm}}$ and k_{p,H_2}, λ_2 and λ_3 become more stable while λ_5 sweeps towards RHP, shown in Fig. 11(a). Decreasing k_{p,H_2} until some values improves the system stability, shown in Fig. 11(b), which move λ_2, λ_3, and λ_5 towards the left half plane (LHP). However, λ_4 which already has a big enough negative value, moves towards RHP. Noting that λ_4 is scaled down. To sum up, tuning the proportional gain of governor controllers (PI_{H_2} and PI_{cm}) is helpful for stabilizing the system as better damping is observed, i.e., the dominant eigenvalues move further toward LHP.

In Table II, λ_{15} and λ_{10} which are less damped modes according to Fig. 9(a), are impacted by v_{dc} and $X_{\text{b,v}}$, where the latter is the auxiliary voltage error state. The relevant PFs are displayed in pink in Table II. Fig. 12 illustrates the movement of the critical eigenvalues with respect to varying PI_{vb}'s control parameters, i.e., voltage control loop parameters. The most critical mode λ_{10}, whose its value shifts to RHP by increasing the load power in Fig. 9(a), moves in a negative direction, i.e., LHP by increasing $k_{\text{pv,b}}$. Hence, the HPS is damped better, and the stability margin increases. However, it's feasible to raise $k_{\text{pv,b}}$ within certain limits, given that doing so causes the movement of λ_{12} towards RHP, as shown in Fig. 12(a). Decreasing $k_{\text{iv,b}}$ also leads to λ_9, λ_{10}, and λ_{12} shifting to the left as shown in Fig. 12(b), which shows less impact in the stability than $k_{\text{pv,b}}$ does. Overall, it can be

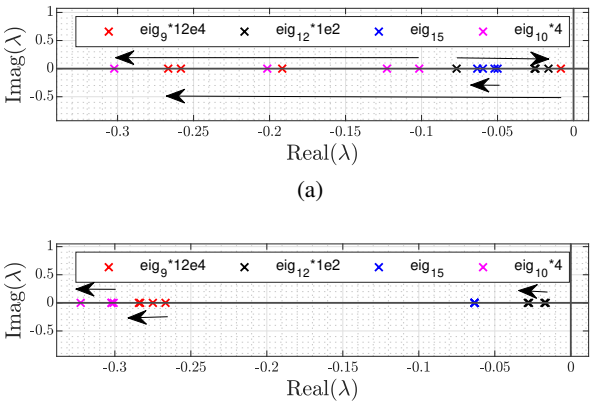

Fig. 12. Eigenvalue movements in scenario I at the operating point of 600kW with respect to: (a) $k_{pv,b}$ variation (increase) from 1 to 10 with $k_{iv,b}$ constant at 525e2, (b) $k_{iv,b}$ movement (decease) from 525e2 to 525 with $k_{pv,b}$ constant at 10, to design the converter's voltage loop parameters.

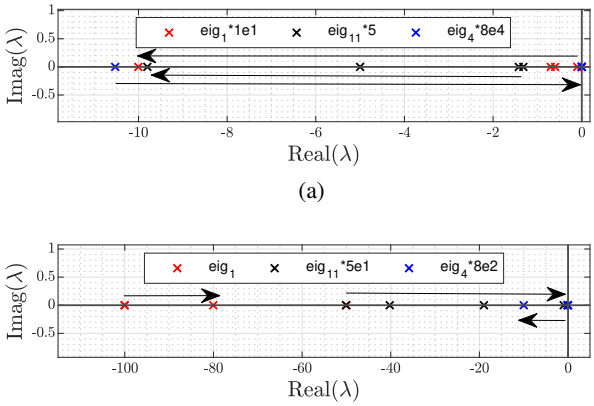

Fig. 13. Eigenvalue movements in scenario II at the operating point of 600kW with respect to varying: (a) $k_{p,cm}$ increases from 1e1 to 3.3e1 with k_{p,H_2} constant at 66, (b) k_{p,H_2} increases from 66 to 5e2 with $k_{p,cm}$ constant at 3.3e1, to design the governor parameters.

TABLE III
SENSITIVITY OF CRITICAL DOMINANT MODES IN SCENARIO II

Mode i	P_{H_2}	P_{O_2}	i_{fc}	$X_{\text{fc,v}}$	$X_{\text{fc,i}}$	v_{dc}
λ_1	0.5573	0.698	0.021	0	0	0
λ_2	0	0	0.9911	0.9472	0.54	0.2811
λ_4	0.988	0.041	0.002	0	0	0
λ_5	0	0	0.094	0.9554	0.8409	0.05
λ_7	0	0	0.503	0.63	0.988	0
λ_{11}	0	0.9472	0	0	0	0
λ_{14}	0	0	0.96	0.8309	0.263	0.9011

concluded that the proportional gain of the voltage controller, i.e., $k_{\text{pv,b}}$ significantly impacts the system stability.

Table III lists the state variables that impact system stability most in scenario II, derived by A_{II}. The modes λ_1, λ_4, and λ_{11} are sensitive to the FC's governor state variables, i.e., P_{H_2}, P_{O_2}, and i_{fc}. The relevant PFs are shown within the boxes in Table III. This demonstrates the coupling between modes related to the governor and FC current state variable i_{fc}. Fig. 13 depicts the mentioned eigenvalues movement by changing the governor's proportional gains, i.e., $k_{\text{p,cm}}$ and k_{p,H_2}. The increase of $k_{\text{p,cm}}$ will significantly compromise the damping since the dominant modes λ_1, and λ_{11} move toward LHP, while λ_4 moves toward RHP. Increasing k_{p,H_2} leads to the opposite direction movement. The control parameters relevant to PI_{O_2} under both scenarios have been investigated, while its contribution to the system stability is insignificant compared to PI_{cm} and PI_{H_2}.

According to Fig. 9(b) the most critical eigenvalues were λ_2 and λ_{14}, that moved towards RHP. These modes with their highest PFs are highlighted in pink in Table III. It can be seen that these modes are sensitive to v_{dc}, $X_{\text{fc,v}}$, and i_{fc}. Fig. 14 shows eigenvalues for the case where control parameters of $PI_{\text{pv,fc}}$ are varied. It is seen that two critical modes λ_2 and λ_{14} move significantly toward LHP when $k_{\text{pv,fc}}$ increases, while λ_5 and λ_7 move toward RHP. These results also can be verified by Table III where these modes are sensitive to $X_{\text{fc,i}}$, and $X_{\text{fc,v}}$. The relevant PFs are highlighted in blue in Table III. The root-locus analysis demonstrates the feasibility and efficacy

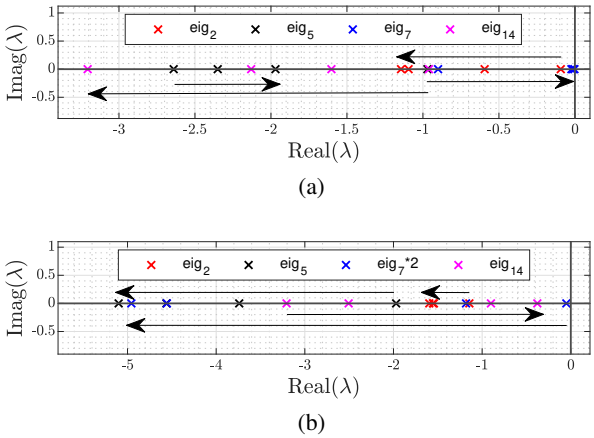

Fig. 14. Eigenvalue movements in scenario II at the operating point of 600kW with respect to: (a) $k_{\text{pv,fc}}$ increases from 1 to 1.25e1 with $k_{\text{iv,fc}}$ constant at 0.77e3, (b) $k_{\text{iv,fc}}$ decreases from 0.77e3 to 0.77 with $k_{\text{pv,fc}}$ constant at 1.25e1, to design the converter's voltage loop parameters.

of the modal analysis to derive the state contribution to the selected modes, which, in turn, enhances the design of control parameters.

The subsystem's states which are in voltage mode control, contribute to the system stability with a coupling between the controller's parameters and the dc subsystem state. This is because of the coupling exist between HPS subsystems, i.e., $[A_{fc/dc}]$, $[A_{dc/fc}]$, $[A_{Batt/dc}]$, and $[A_{dc/Batt}]$. The evidence for this is that eigenvalues associated with dc bus voltage and voltage error dynamics moved when proportional gains of the voltage loop controller were changed. To investigate the coupling feature further, the PFs are plotted against the gains $k_{\text{pv,b}}$ and $k_{\text{pv,fc}}$.

Fig. 15(a) shows the PFs of the state variables in λ_{10} as a function of the battery's outer loop voltage control proportional gain, i.e., $k_{\text{pv,b}}$. Four states from HPS are chosen because of their higher PF values shown in Table II, which are associated with the different HPS's subsystems. It is observed that the participation of the voltage error state $X_{\text{b,v}}$ grows as the gain increases. Also, high $k_{\text{pv,b}}$ causes a further coupling

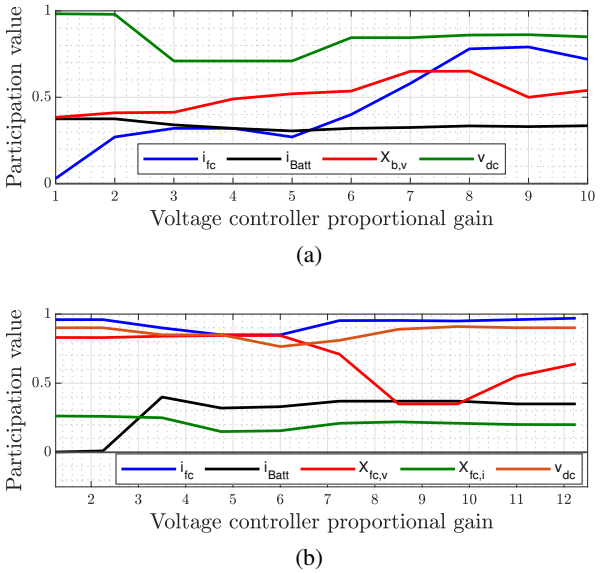

Fig. 15. Participation trace of (a) HPS states (shown in Table. II for scenario I) as a function of the battery outer loop voltage controller proportional gain $K_{\text{pv,b}}$ for λ_{10}, and (b) HPS's states (shown in Table. III for scenario II) as a function of the FC outer loop voltage controller proportional gain $k_{\text{pv,fc}}$ for λ_{14}.

between i_{Batt} and i_{fc} with the dc bus voltage dynamics.

Fig. 15(b) depicts the PFs of state variables (Table III) in eigenvalue λ_{14} as a function of the FC voltage loop's proportional gain, i.e., $k_{\text{pv,fc}}$, for a fixed set of other control parameters. The same as scenario I, the coupling between current states and dc bus voltage dynamics increases with higher $k_{\text{pv,fc}}$. This demonstrates the effect of the dc bus voltage state v_{dc} as a bridge between the dc subsystems' coupling. These couplings must be considered when designing the HPS.

V. Simulations and Experimental Validation

In support of the stability analysis in the previous section, time-domain simulations and experiments are done in this section.

A. Time Domain Simulation

A small-scaled tugboat power plant is configured as the target vessel for the verification of the root-locus analysis. It is a typical HPS as shown in Fig. 4 with the system parameters listed in Table. I. The simulation results have been carried out for the governor design and the voltage controller design under both control scenarios and different case studies.

1) Fuel cell governor: First, simulations are done to verify the governor root-locus analysis (see Fig. 11) to examine the control parameters of PI_{cm} and PI_{H_2} as shown in Fig. 16 based on the FC ramp-rate (20 A/s). Fig. 16(a) depicts the oxygen excess ratio λ_{O_2} variation when the load power ramps up from 25% to 100% load at $t = 4s$. The simulation results are aligned with the root-locus analysis for the governor parameters selection. It is observed that the control parameters of $k_{\text{p,cm}} = 0.02$ and $k_{p,H_2} = 1.2e1$ can provide more damping in λ_{O_2} and also lower undershoot when i_{fc}

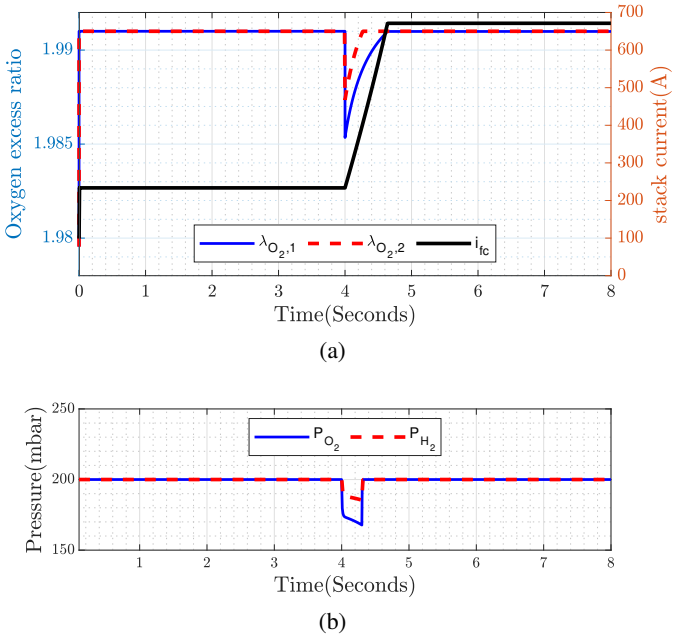

Fig. 16. Time-domain verification of the governor tuning when a ramp change from 0.25% to 100% load power (40A/s) is applied at $t = 4s$ in scenario I: (a) oxygen excess ratio with $k_{\text{p,cm}} = 1$ and $k_{p,H_2} = 1.2e1$ results in $\lambda_{O_2,1}$, and $k_{\text{p,cm}} = 0.02$ and $k_{p,H_2} = 2e1$ results in $\lambda_{O_2,2}$ (better damping) respectively, (b) pressure results with the damped $\lambda_{O_2,2}$.

ramps up. Moreover, according to the sensitivity analysis in both scenarios, the coupling existed between modes related to the FC governor state variables and FC current i_{fc}, as can be observed from Table. II and Table. III. The latter is demonstrated with Fig. 16(b), where pressures instantaneously follow i_{fc} with the acceptable drop when the power ramp is applied at $t = 4s$. The governor performance verification under a dynamic marine load profile for both scenarios are given in Fig. 16, where P_{H_2} follows P_{O_2} in a flow-controlled design. The load profile (see Fig. 25) is designed as high magnitude step-up, step down, ramp-up and ramp-down cycles, indicating vessel maneuvering with different speeds, acceleration, and docking.

2) Voltage controller: The root-locus analysis for the voltage control loop parameters is verified under 3 case studies. According to Fig. 12 and Fig. 14, voltage controller parameters, i.e., $PI_{\text{pv,b}}$ and $PI_{\text{pv,fc}}$ contribute to the system voltage stability during scenario I and scenario II respectively. In the first case study (Case1), the load power is increasing step-wise from 25% to 100% load at $t = 1s$. Verification of the root-locus analysis for $PI_{\text{pv,b}}$ during scenario I, stable and unstable system, is given in Fig. 18(a) and (b) respectively. Both time-domain simulations verify the root-locus analysis, where the dc bus voltage oscillations are well-damped with the selected $PI_{\text{pv,b}}$'s parameters, i.e., $k_{\text{pv,b}}$ and $k_{\text{iv,b}}$. In Fig. 18(b) After $t = 1s$ instability is observed when $k_{\text{pv,b}}$ is increased, as was shown in Fig. 12 (a), where λ_{12} moved towards RHP with increasing $k_{\text{iv,b}}$. The experiment is repeated for scenario II, to demonstrate the root-locus analysis results in Fig. 14 for the control parameters of $PI_{\text{pv,fc}}$. Fig. 19 demonstrates that the control parameters of $k_{\text{pv,fc}} = 1.25e1$ and $k_{\text{iv,fc}} = 0.77$ can

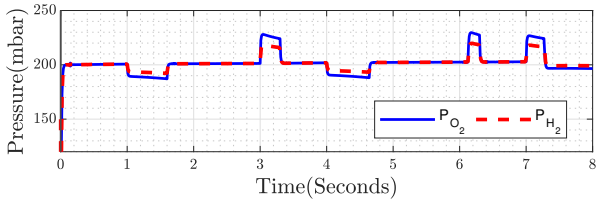

(a)

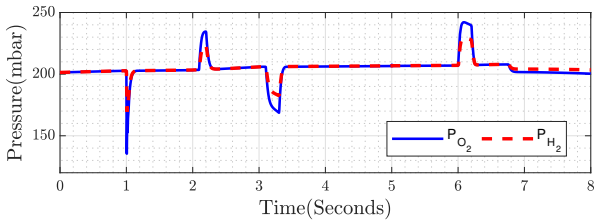

(b)

Fig. 17. Time-domain verification for the governor performance with the governor control parameters obtained within root-locus analysis, showing the variations of hydrogen and oxygen pressure for the ship load profile shown in Fig. 25: (a) scenario I with $k_{\text{p,cm}} = 0.02$ and $k_{p,H_2} = 2e1$, and (b) scenario II with $k_{\text{p,cm}} = 3.3e1$ and $k_{p,H_2} = 66$.

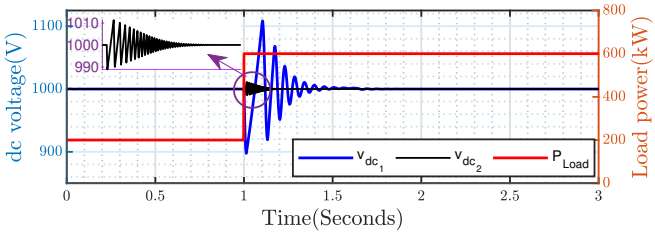

(a)

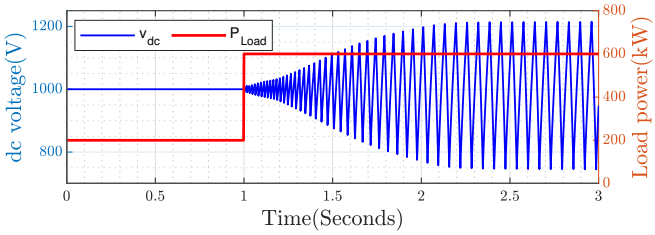

(b)

Fig. 18. Case1: Time-domain verification results for dc bus voltage v_{dc} variation in scenario I for the step-wise load changes P_{load} from 25% load to 100% at $t = 1s$: (a) with $k_{pv,b} = 1$ and $k_{iv,b} = 525e2$ results in v_{dc_1} and with $k_{pv,b} = 10$ and $k_{iv,b} = 525$ results in v_{dc_2} (better damping), (b) unstable case with $k_{pv,b} = 15$ and $k_{iv_b} = 525$.

provide better damping in dc bus voltage v_{dc}.

For the second case study, i.e., Case2 (see Fig. 20 and Fig. 21), the load power ramps up from 25% to 100% load at $t = 1s$, with the duration of $t = 0.25s$, i.e., 80A/s, which is steeper than the FC's ramp rate, i.e., 20A/s. The voltage stability of the HPS was impacted by the proportional gain of the voltage control loop in both scenarios examined in Case1. In this context to support the analytical analysis, the dc bus voltage v_{dc} variation is studied under $k_{\text{pv,b}}$ and $k_{\text{pv,fc}}$ changes. During scenario I, the battery with high power density controls v_{dc}; hence, the fast ramp-up load power is

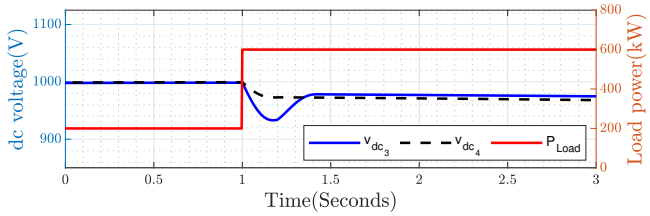

Fig. 19. Case1: Time-domain verification results for dc bus voltage v_{dc} variation in scenario II for the step-wise load changes P_{Load} from 25% load to 100% at $t = 1s$ with $k_{\text{pv,fc}} = 1.25$ and $k_{\text{iv,fc}} = 0.77$ results in v_{dc_3} and with $k_{\text{pv,fc}} = 1.25e1$ and $k_{\text{iv,fc}} = 0.77$ results in v_{dc_4} (better damping)

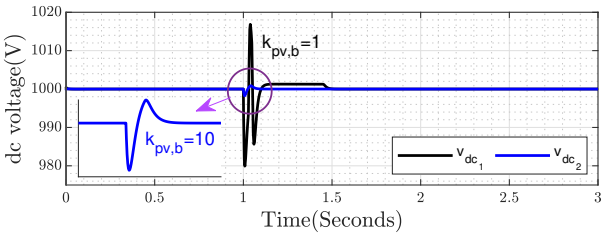

Fig. 20. Case2: Time-domain verification results for the dc bus voltage v_{dc} variation in scenario I for the ramp-up load changes P_{load} from 25% load to 100% at $t = 1s$ within $0.25s$, i.e., 80A/s with $k_{\text{pv,b}} = 1$ and $k_{\text{iv,b}} = 525$ results in v_{dc_1}, and with $k_{\text{pv,b}} = 10$ and $k_{\text{iv,b}} = 525$ results in v_{dc_2}.

supplied by the HPS without a steady-state voltage drop. However, the dynamic response of v_{dc} has more variation when FC regulates v_{dc}, illustrated in Fig. 21. This demonstrates the effect of $k_{\text{pv,fc}}$'s tuning on the system behavior. Moreover, the latter demonstrates the analytical analysis shown in Fig. 14(a), where λ_7 moved toward RHP by increasing of $k_{\text{pv,fc}}$.

Fig. 22 demonstrates the v_{dc} dynamic responses while varying $k_{\text{pv,b}}$ and $k_{\text{pv,fc}}$ under the transient ship load profile as the case study 3 (Case3). The load profile includes high magnitude ramp-up, step-down, step-up and ramp-down cycles. The magnitudes are designed the same as Case1 and Case2. As expected from the previously detailed analytical analysis, Case3 verifies that the HPS is impacted by the changes in the proportional gain of the voltage control loop in both scenarios. The $k_{\text{pv,b}}$ and $k_{\text{pv,fc}}$ values in Case3 have been selected the same as their values examined in Case1 and Case2, and the same dynamic behaviour has been seen during the load transients. The case studies' results are also

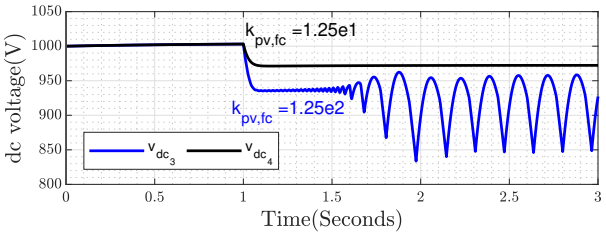

Fig. 21. Case2: Time-domain verification results for the dc bus voltage v_{dc} variation in scenario II for the ramp-up load changes P_{load} from 25% load to 100% at $t = 1s$ within $0.25s$, i.e., 80A/s with $k_{\text{pv,fc}} = 1.25e2$ and $k_{\text{iv,fc}} = 0.77$ results in v_{dc_3}, and with $k_{\text{pv,fc}} = 1.25e1$ and $k_{\text{iv,fc}} = 0.77$ results in v_{dc_4}.

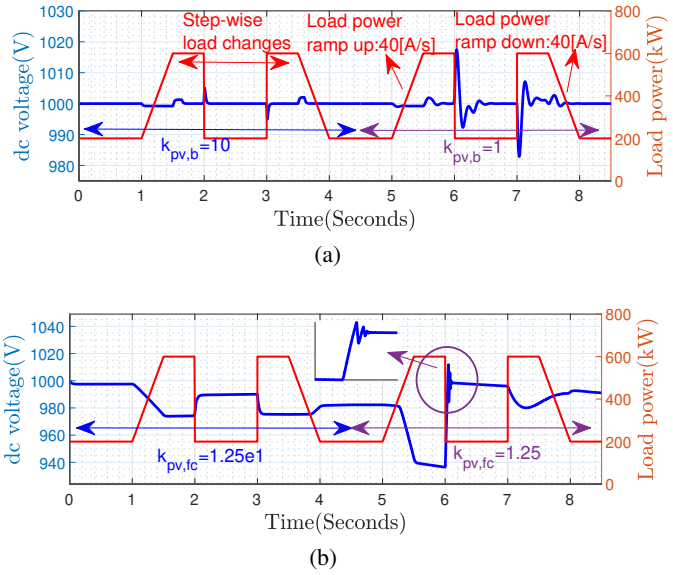

Fig. 22. Case3: Time-domain verification results for the dc bus voltage v_{dc} variation in (a) scenario I with variation of control parameter $k_{\mathrm{pv,b}}$ from 10 to 1, and (b) scenario II with variation of control parameter $k_{\mathrm{pv,fc}}$ from 1.25e1 to 1.25 under the same sample marine load profile including ramp-up, step-wise, and ramp-down load changes, as well as under low and high cruising speed.

aligned with the sensitivity analysis illustrated in Table. II and Table. III. According to the tables, v_{dc} and $X_{\mathrm{b,V}}$ state variables contribute in λ_{10} in scenario I, and v_{dc} and $X_{\mathrm{fc,V}}$ state variables contribute strongly in λ_{14} in scenario II. These particular system modes moved previously to RHP when the load power increased (see Fig. 9).

Comparison of two implemented control scenarios demonstrates the impact of the slower dynamic response of the FC comparing to the battery in high power load transients. According to Fig. 18- Fig. 22, when power load increases 75%, v_{dc} only has 1% variation in scenario I, and backs to a steady-state value within 200ms, while v_{dc} experienced 4% steady-state error in scenario II within 400ms for the step-up load power, and 100ms for the 80A/s ramp-up load change. In the actual shipboard HPS operation, to ensure the system stability and dynamic responses, the FCs are usually operated under current mode to provide the average shipload power supply, and batteries are under voltage control mode to maintain a stable system dc voltage (scenario I).

B. HIL Verification

System studies and tuning are time-consuming, expensive and potentially dangerous if against a real hardware system. Therefore, a hardware-in-the-loop (HIL) setup is expected to provide the real-time response of the system while at the same time minimizing the development cycle and cost.

In this stability study, a hybrid shipboard power HIL plant is set up to verify the system's dynamic behaviour. The HPS HIL platform is built in the Nanyang Technological University (NTU) Mechatronics lab. The system-level power plant model, including the power devices (FCs and batteries), the dc-dc converters and the controllable load are modelled with Matlab/Simulink environment, and run on a real-time Speed-

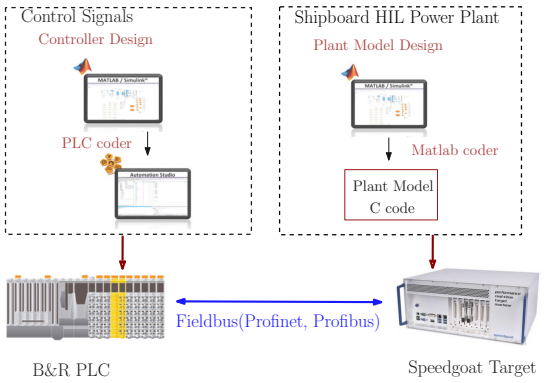

Fig. 23. HIL topology scheme.

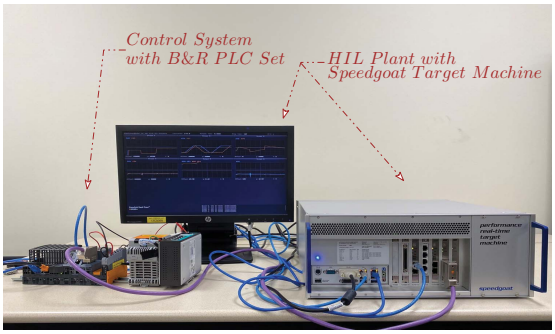

Fig. 24. HIL setup in lab environment.

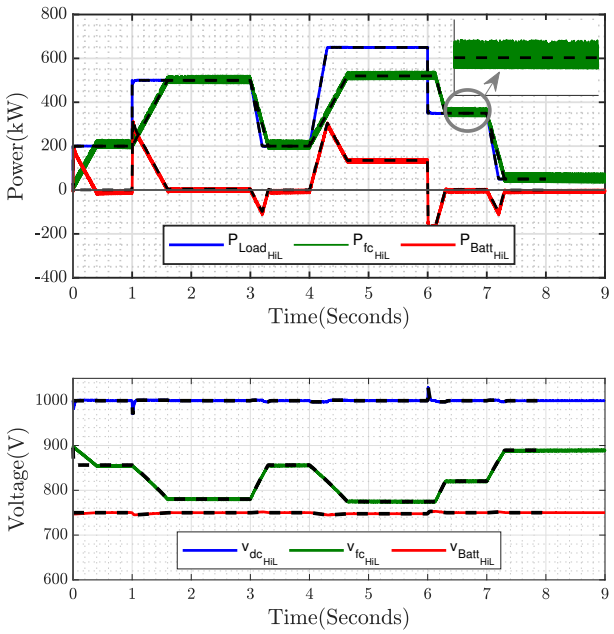

Fig. 25. Validation test for the scenario I: to compare the developed HPS's performance between the simulation model and the HIL plant target under dynamic ship load profile. Note that the dashed lines indicate the simulation model's response.

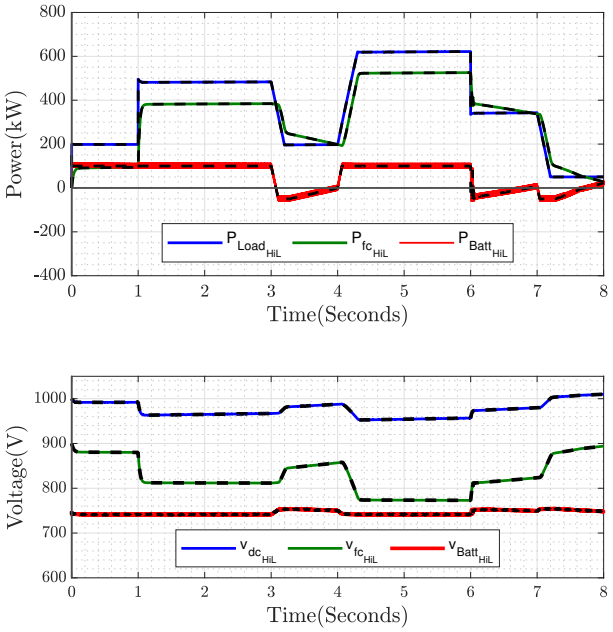

Fig. 26. Validation test for the scenario II: to compare the developed HPS's performance between the simulation model and the HIL plant target under dynamic ship load profile. Note that the dashed lines indicate the simulation model's response.

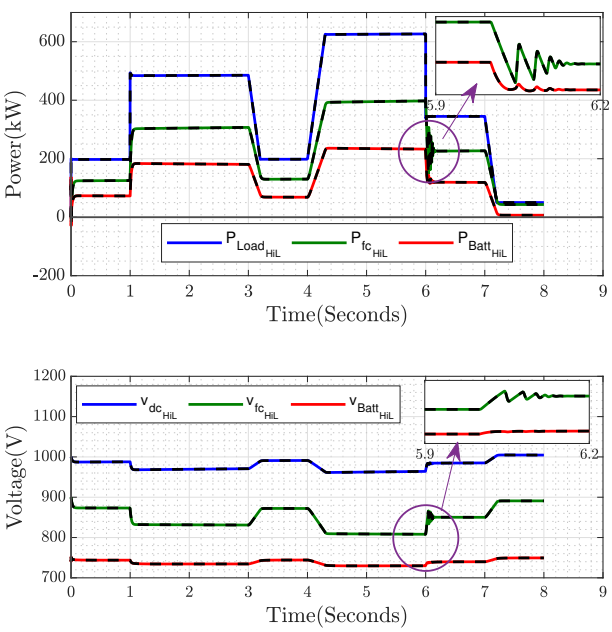

Fig. 27. Validation test: to compare the HPS's response between simulation model and HIL plant target when FC and battery are in droop control with the FC droop rate 1% and the battery droop rate 5%. Note that the dashed lines indicate the simulation model's response.

TABLE IV
CONTROL PARAMETERS USED FOR THE HIL POWER PLANT

Name	Scenario I		Scenario II	
Hydrogen governor	k_{p,H_2}	2e1	k_{p,H_2}	66
Hydrogen governor	k_{i,H_2}	14	k_{i,H_2}	12e1
Oxygen governor (inner loop)	k_{p,O_2}	1.6e1	k_{p,O_2}	1.4e1
Oxygen governor (inner loop)	k_{i,O_2}	77e-1	k_{i,O_2}	77e-1
Oxygen governor (outer loop)	$k_{p,cm}$	2e-2	$k_{p,cm}$	3.3e1
Oxygen governor (outer loop)	$k_{i,cm}$	3e2	$k_{i,cm}$	3e2
FC converter (inner loop)	$k_{\text{pi,fc}}$	10e1	$k_{\text{pi,fc}}$	5e2
FC converter (inner loop)	$k_{\text{ii,fc}}$	1e2	$k_{\text{ii,fc}}$	52e2
FC converter (outer loop)	–	–	$k_{\text{pv,fc}}$	1.25e1
FC converter (outer loop)	–	–	$k_{\text{iv,fc}}$	77e-2
Battery converter (inner loop)	$k_{\text{pi,b}}$	1e2	$k_{\text{pi,b}}$	15e1
Battery converter (inner loop)	$k_{\text{ii,b}}$	3e2	$k_{\text{ii,b}}$	2e2
Battery converter (outer loop)	$k_{\text{pv,b}}$	10	–	–
Battery converter (outer loop)	$k_{\text{iv,b}}$	525	–	–

goat target machine, which provides a real-time simulation of the plant dynamics as well as the industrial communication interface with Fieldbus protocols according to class rules [27]. The control signals, including power load profile, voltage and current references, are deployed to a B&R X20CP3586 programmable logic controller (PLC). The topology diagram of the HIL platform can be found in Fig. 23. The Profinet is selected as the communication connection between the PLC controller and the Speedgoat HIL plant. The HIL testbed setup in the lab environment is shown in Fig. 24.

In the validation test, the ship load profile is designed as the ramp-up, ramp-down, step-up and step-down cycles, which impose the short-term transients for the stability analysis assessment under the small perturbations. The load model cycle's magnitudes match those utilized in the time-domain simulation for Case1, Case2, and Case3. Therefore, the overall performance of the analytical stability analysis, time-domain simulation, and real-time HIL simulator are examined to be aligned. The control parameters that were verified during the time-domain simulation, and are used for the HIL simulator have been listed in Table. IV. As depicted in Fig. 25-27, the test outcomes illustrate a clear alignment between the simulation results generated by the Simulink model and the outcomes from the HIL plant. When the load increases 60% in $t = 1s$, v_{dc} has 1% variation in scenario I (see Fig. 25), and no voltage variations have been observed while the load follows a ramp rate of 80A/s in $t = 4s$. While v_{dc} experiences 4% steady-state error in scenario II in $t = 1s$ within 100ms (see Fig. 26), and 5% steady-state error in $t = 4s$ within 300ms. The findings are aligned with the time-domain simulation done in Case1 and Case2.

The HPS performance in droop mode is shown in Fig. 27 to compare with scenario I and scenario II. The tests match the stability analysis, in which scenario I showed less dc bus voltage deviation compared to the scenario II. The transient rise time and steady-state power and voltage output for both FC and battery power sources of the Simulink model align with the HIL system. However, the output from the HIL power plant is slightly more oscillatory compared with the pure simulation results, which can be referred to Fig. 25 and Fig. 26. The main reason is that the HIL system is a discretization conversion from the Simulink model. The performance of the HIL plant depends greatly on the computational capacity of the target machine processor, PLC task cyclic time, and the communication transmission bandwidth. The minor oscillation is acceptable.

To further analyze the battery operations in both control scenarios, the SOC is illustrated in Fig. 28. When the battery

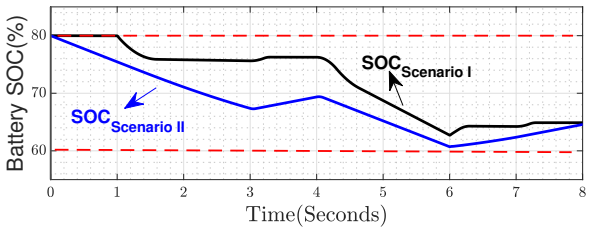

Fig. 28. The battery SOC variation in two implemented scenarios under the same ship load profile used for the HIL verification.

converter control is designed with a dual control loop (controlling the dc bus voltage) in Fig. 28, the change of SOC is smoother than the other case. In both control schemes SOC remains between the defined boundary, that is 60%-80%. The safe working range for a battery shall be between 10-90%. Over-charging or discharging will impact the battery life-cycle and system operation conditions.

VI. Conclusion

This paper focused on the stability analysis for FC-powered vessels and to map the dynamic interactions between the source and load subsystems. An analytical model was developed and linearized around the operating points to assess the HPS stability under small perturbations. The comprehensive modal analysis was employed to identify the relative contribution of a system's state to the selected modes through the PF calculation, which in turn simplified the control parameter selection to expand the stable operating region of the HPS. By employing sensitivity analysis the impact of control parameters of the governor and converter controllers on the HPS stability was investigated. Two control scenarios for the FC and battery converter were considered, provided valuable insights about expected FC dynamic interactions in marine hybrid power system.

From the modal analysis, it was found that the PI-based control parameters of the converter with the voltage control loop had strong impact on the HPS stability and the eigenvalue change tendency. The study demonstrated PF of 0.9 between the dc bus voltage and the critical modes within 15% deviation by changes in the voltage controller's proportional gain, caused a further coupling between subsystems' current state variable parameters and the dc bus voltage dynamics. This is because the eigenvalues associated with the dc bus and load subsystem behaves as a bridge between other dc subsystems. Additionally, a strong coupling existed between governor dynamics and the FC's current state, demonstrating the efficacy of considering the FC's mass balance dynamics in the HPS stability analysis. On the whole, within FC's converter in current mode control considering FC's ramp rate limit, the dc bus voltage had only 1-2% variation during transients. However 4-5% steady-state error was recorded within FC's converter in voltage mode control. The HPS model was verified against time-domain simulations and a hardware-in-the-loop (HIL) setup to replicate the real-time system behaviour.

The presented stability analysis was examined according to the power devices data-sheet provided by the product suppliers. The system stability is not able to guarantee if the system constraints are exceeded, such as the power and ramp rate limits. Moreover, for future research in the system-level stability analysis, the control design can also include the HPS's physical parameters, particularly the converter inductance, and dc bus capacitor. Finally, HIL was based on the converter averaged model due to the limitation of the target machine CPU capability. A further test might consider to be engaged with a real hardware-based plant.

References

[1] A. Haxhiu, A. Abdelhakim, S. Kanerva, and J. Bogen, "Electric Power Integration Schemes of the Hybrid Fuel Cells and Batteries-Fed Marine Vessels—An Overview," *IEEE Transactions on Transportation Electrification*, vol. 8, no. 2, pp. 1885–1905, Jun. 2022.

[2] I. M. Organization. (2018) Reducing greenhouse gas emissions from ships. [Online]. Available: https://www.imo.org/.

[3] M. Zadeh and P. Ghimire, *Shipboard DC Hybrid Power Systems*, 2023, pp. 475–497.

[4] P. Ghimire, M. Zadeh, E. Pedersen, and J. Thorstensen, "Dynamic Modeling, Simulation, and Testing of a Marine DC Hybrid Power System," *IEEE Transactions on Transportation Electrification*, vol. 7, no. 2, pp. 905–919, Jun. 2021.

[5] N. Shakeri, M. Zadeh, and J. Bremnes Nielsen, "Hydrogen Fuel Cells for Ship Electric Propulsion: Moving Toward Greener Ships," *IEEE Electrification Magazine*, vol. 8, no. 2, pp. 27–43, Jun. 2020.

[6] A. Riccobono and E. Santi, "Comprehensive Review of Stability Criteria for DC Power Distribution Systems," *IEEE Transactions on Industry Applications*, vol. 50, no. 5, pp. 3525–3535, Sep. 2014.

[7] S. Leitner, M. Yazdanian, A. Mehrizi-Sani, and A. Muetze, "Small-Signal Stability Analysis of an Inverter-Based Microgrid With Internal Model-Based Controllers," *IEEE Transactions on Smart Grid*, vol. 9, no. 5, pp. 5393–5402, Sep. 2018.

[8] U. Javaid, F. D. Freijedo, D. Dujic, and W. van der Merwe, "Dynamic Assessment of Source–Load Interactions in Marine MVDC Distribution," *IEEE Transactions on Industrial Electronics*, vol. 64, no. 6, pp. 4372–4381, Jun. 2017.

[9] M. K. Zadeh, R. Gavagsaz-Ghoachani, J.-P. Martin, B. Nahid-Mobarakeh, S. Pierfederici, and M. Molinas, "Discrete-Time Modeling, Stability Analysis, and Active Stabilization of DC Distribution Systems With Multiple Constant Power Loads," *IEEE Transactions on Industry Applications*, vol. 52, no. 6, pp. 4888–4898, Nov. 2016.

[10] U. Javaid, F. D. Freijedo, W. van der Merwe, and D. Dujic, "Stability Analysis of Multi-Port MVDC Distribution Networks for All-Electric Ships," *IEEE Journal of Emerging and Selected Topics in Power Electronics*, vol. 8, no. 2, pp. 1164–1177, Jun. 2020.

[11] DNV, "Safety, operation and performance of grid-connected energy storage systems," DNV-RP-0043, Oct, 2021.

[12] G. Sulligoi, A. Vicenzutti, V. Arcidiacono, and Y. Khersonsky, "Voltage Stability in Large Marine-Integrated Electrical and Electronic Power Systems," *IEEE Transactions on Industry Applications*, vol. 52, no. 4, pp. 3584–3594, Jul. 2016.

[13] S. Sudhoff, S. Glover, P. Lamm, D. Schmucker, and D. Delisle, "Admittance space stability analysis of power electronic systems," *IEEE Transactions on Aerospace and Electronic Systems*, vol. 36, no. 3, pp. 965–973, Jul. 2000.

[14] D. Park and M. Zadeh, "Dynamic Modeling, Stability Analysis, and Power Management of Shipboard DC Hybrid Power Systems," *IEEE Transactions on Transportation Electrification*, vol. 8, no. 1, pp. 225–238, Mar. 2022.

[15] G. Tzounas, I. Dassios, and F. Milano, "Modal Participation Factors of Algebraic Variables," *IEEE Transactions on Power Systems*, vol. 35, no. 1, pp. 742–750, Jan. 2020.

[16] F. Gao, X. Zheng, S. Bozhko, C. I. Hill, and G. Asher, "Modal Analysis of a PMSG-Based DC Electrical Power System in the More Electric Aircraft Using Eigenvalues Sensitivity," *IEEE Transactions on Transportation Electrification*, vol. 1, no. 1, pp. 65–76, Jun. 2015.

[17] F. Barbir, "PEM Fuel Cells," in *Fuel Cell Technology: Reaching Towards Commercialization*, ser. Engineering Materials and Processes, N. Sammes, Ed. London: Springer, 2006.

[18] J. Sun and I. Kolmanovsky, "Load governor for fuel cell oxygen starvation protection: a robust nonlinear reference governor approach," *IEEE Transactions on Control Systems Technology*, vol. 13, no. 6, pp. 911–920, Nov. 2005.

[19] N. Shakeri, M. Zadeh, and J. Bruinsma, "Dynamic Modeling and Validation of a Fuel Cell-Based Hybrid Power System for Zero-Emission Marine Propulsion: an Equivalent Circuit Model Approach," *IEEE Journal of Emerging and Selected Topics in Industrial Electronics*, Early Access.

[20] A. Haxhiu, J. Kyyrä, R. Chan, and S. Kanerva, "Improved Variable DC Approach to Minimize Drivetrain Losses in Fuel Cell Marine Power Systems," *IEEE Transactions on Industry Applications*, vol. 57, no. 1, pp. 882–893, Jan. 2021.

[21] B. Zahedi and L. E. Norum, "Modeling and Simulation of All-Electric Ships With Low-Voltage DC Hybrid Power Systems," *IEEE Transactions on Power Electronics*, vol. 28, no. 10, Oct. 2013.

[22] R. W. Erickson and D. Maksimovic, *Fundamentals of Power Electronics. Norwell, Mass: Kluwer Academic*, 2001.

[23] "IEEE Recommended Practice for 1 kV to 35 kV Medium-Voltage DC Power Systems on Ships," *IEEE Std 1709-2018 (Revision of IEEE Std 1709-2010)*, vol. 8, no. 2, pp. 1–54, Dec. 2018.

[24] J. T. Pukrushpan, H. Peng, and A. G. Stefanopoulou, "Control-Oriented Modeling and Analysis for Automotive Fuel Cell Systems," *Journal of Dynamic Systems, Measurement, and Control*, vol. 126, no. 1, pp. 14–25, Apr. 2004.

[25] Z. Gong et al, "A 1 + 1-d multiphase proton exchange membrane fuel cell model for real-time simulation," *IEEE TTransactions on Transportation Electrification*, vol. 8, no. 2, pp. 2928–2944, 2022.

[26] N. Shakeri and M. Zadeh, "Dynamic Modelling of Fuel Cell Systems for Electric Propulsion," in *IECON 2021 – 47th Annual Conference of the IEEE Industrial Electronics Society*, Oct. 2021, pp. 1–6.

[27] W. Chen, K. Tai, M. Lau, A. Abdelhakim, R. R. Chan, A. K. Ådnanes, and T. Tjahjowidodo, "DC-Distributed Power System Modeling and Hardware-in-the-Loop (HIL) Evaluation of Fuel Cell-Powered Marine Vessel," *IEEE Journal of Emerging and Selected Topics in Industrial Electronics*, vol. 3, no. 3, pp. 797–808, Jul. 2022.

[28] M. Hossain, S. Saha, M. T. Arif, A. M. T. Oo, N. Mendis, and M. E. Haque, "A Parameter Extraction Method for the Li-Ion Batteries With Wide-Range Temperature Compensation," *IEEE Transactions on Industry Applications*, vol. 56, no. 5, pp. 5625–5636, Sep. 2020.

[29] F. Zenith and S. Skogestad, "Control of fuel cell power output," *Journal of Process Control*, vol. 17, no. 4, pp. 333–347, Apr. 2007.

[30] M. Chen and G. Rincon-Mora, "Accurate electrical battery model capable of predicting runtime and I-V performance," *IEEE Transactions on Energy Conversion*, vol. 21, no. 2, pp. 504–511, Jun. 2006.

[31] N. Bottrell, M. Prodanovic, and T. C. Green, "Dynamic Stability of a Microgrid With an Active Load," *IEEE Transactions on Power Electronics*, vol. 28, no. 11, pp. 5107–5119, Nov. 2013.

[32] A. J. Sørensen, "A survey of dynamic positioning control systems," *Annual Reviews in Control*, vol. 35, no. 1, pp. 123–136, Apr. 2011.

LIST OF ABBREVIATIONS

FC	Fuel Cell
PEMFC	Proton Exchange Membrane Fuel Cell
HIL	Hardware-in-the-Loop
H_2	Hydrogen
O_2	Oxygen
ESS	Energy Storage System
dc	Direct Current
HPS	Hybrid Power System
PEs	Power Electronics
PMS	Power Management System
EEC	Electric Equivalent Circuit
PF	Participation Factor
EMS	Energy Management System
SLD	Single Line Diagram
SOC	State of Charge
BoP	Balance of Plant
PWM	Pulse Width Modulation
RHP	Right Half Plane
LHP	Left Half Plane

LIST OF NOMENCLATURES

v_{dc}	dc Bus Voltage
v_{fc}	FC Voltage
i_{fc}	FC current
d_{fc}	FC dc-dc Converter Duty Cycle
P_{H_2}	Hydrogen Partial Pressure
P_{O_2}	Oxygen Partial Pressure
PI_{H_2}	Hydrogen Governor Controller
PI_{O_2}	Oxygen Governor Inner Loop Control
PI_{cm}	Oxygen Governor Outer Loop Control
λ_{O_2}	Oxygen Excess Ratio
X_i	Auxiliary State Variable
P_{cm}	Compressor Partial Pressure
r_{fc}	FC Power Ramp Rate
$\tau_{\text{fc,r}}$	FC Dynamic Time Constant
PI_{vfc}	FC Outer Voltage Loop Control
PI_{ifc}	FC Inner Current Loop Control
v_{Batt}	Battery Voltage
i_{Batt}	Battery current
d_{Batt}	Battery dc-dc Converter Duty Cycle
PI_{vb}	battery Outer Voltage Loop Control
PI_{ib}	battery Inner Current Loop Control
i_{load}	Load Current
P_{load}	Load Power
$k_{\text{dr,fc}}$	FC Droop Rate
$k_{\text{dr,b}}$	Battery Droop Rate
A	State Matrix
B	Input Matrix
p_{ki}	Participation Factor
λ_i	i_{th} System Mode (Eigenvalue)

Nastaran Shakeri received the B.Sc. degree in electrical engineering, in 2015, and the M.Sc. degree in control engineering from Babol Noshirvany University of Technology, Iran, in 2017. She is currently pursuing the Ph.D. degree in Marine Engineering with the Department of Marine Technology, Norwegian University of Science and Technology (NTNU), Trondheim, Norway. Her research interests are the modeling, control, and stability analysis of shipboard hybrid power systems with fuel cells.

Wenjie Chen received her B.Sc. degree in automation from Shanghai Maritime University in Shanghai, China in 2007. And received her M.Sc. degree in electrical engineering from Ecole Polytechnique de l'Université de Nantes, France in 2009. And then she entered ABB (Singapore) to be a research engineer. Since January 2019, she has been working toward a Ph.D. degree in optimization control for power systems under the supervision of Prof. K. Tai from Nanyang Technological University, Singapore, and Prof. T. Tjahjowidodo from Katholieke Universiteit Leuven, Leuven, Belgium.

Mehdi Zadeh (Senior Member, IEEE) received the Ph.D. degree in Electrical Engineering from the Norwegian University of Science and Technology (NTNU), Trondheim, Norway, in 2016. From 2016 to 2017, he was with Zaptec Charger, Stavanger, Norway, where he was working on the development of battery charging systems for electric vehicles based on wide band-gap power electronics. In 2017, he joined the Department of Marine Technology at NTNU, Trondheim, where he is currently a Professor and the director of the Marine Electrification Research Lab. His current research interests include electrification for zero-emission and autonomous shipping, onboard and hybrid DC power systems, offshore renewable energy systems, and sustainable ports. He has taken part in the management of several European, national, and industrial projects, and is currently the work package leader for Power systems and fuel at the SFI Smart Maritime – Norwegian Research-Based Innovation Centre for Improved Energy Efficiency and Reduced Harmful Emissions.

Ahmed Abdelhakim (IEEE S'15-M'18-SM'19) was born in Egypt on April 1, 1990. He received the B.Sc. and the M.Sc. degrees (with Hons.) in electrical engineering from Alexandria University, Egypt, in 2011 and 2013 respectively, and the Ph.D. degree from the University of Padova, Italy, in 2019. He is currently with Epiroc as a Global Electrification Program Manager.

From August 2018 till May 2023, he was with ABB Corporate Research Center in Sweden, where he held several roles as a scientist, senior scientist, and principal scientist. In 2017, he was with Aalborg University, Denmark, as a visiting scholar for ten months, where he was working on several research activities as part of his Ph.D. studies. In January 2015, he joined the University of Padova as a research fellow, where he was working on several research activities for eight months. In 2012, he was with Spiretronics company's R&D team in Egypt, then he was a visiting scholar in Texas A&M university, Qatar. From 2011 to 2014, he was with Alexandria University as a Teaching Assistant, where he helped in teaching several power electronics and power systems courses for the undergraduate students. His major field of interest includes power electronics converters and their applications for energy storage and hydrogen systems for stationary and mobile applications, investigation of new power converter topologies, and application of wide-bandgap (WBG) semiconductor devices (GaN/SiC) for high frequency and high-power density power converters.

Dr. Abdelhakim has received first classified excellent Ph.D. dissertation award from Società Italiana di Electronica (SIE'19) among Italian universities in 2019. He is also serving as an Associate Editor with IEEE Transaction on Industrial Electronics.

Asgeir J. Sørensen obtained the M.Sc. degree in Marine Technology in 1988 at NTNU, and the Ph.D. degree in Engineering Cybernetics at NTNU in 1993. Since 1999 Sørensen has held the position of Professor of Marine Control Systems at the Department of Marine Technology, He is currently director of NTNU VISTA CAROS. Sørensen is engaged in bringing fundamental research results into value creation by innovations and entrepreneurships.

Kang Tai received his B.Eng. in Mechanical Engineering from the National University of Singapore and his Ph.D. from Imperial College, London. He is currently an Associate Professor in the School of Mechanical and Aerospace Engineering, at Nanyang Technological University, Singapore. His research interests include optimization, evolutionary computation, mathematical/empirical modeling of industrial processes, and analysis of interdependencies, risks, and vulnerabilities in critical infrastructure networks.